PREPARATION OF LAYERED CARBON-BASED NANOMATERIALS VIA THERMOCHEMICAL TREATMENT

by

Michael Kwabena Opoku, BSc, MS, PhD

A dissertation submitted to the Graduate Council of
Texas State University in partial fulfillment
of the requirements for the degree of
Doctor of Philosophy
with a Major in
Materials Science, Engineering and Commercialization
May 2019

Committee Members:

Gary W. Beall, Chair

Christopher P. Rhodes

William T. Chittenden

Alexander Zakhidov

L. Kevin Lewis

FAIR USE AND AUTHOR'S PERMISSION STATEMENT

Fair Use

Duplication Permission

DEDICATION

I dedicate this dissertation to my unborn children and the amazing people of Ghana.

ACKNOWLEDGEMENTS

I would like to acknowledge my research advisor, Regents' Professor Gary W. Beall for his time and assistance throughout my studies. Professor Beall is undoubtedly the best advisor, and there is no way I could have done this without his continuous support and dedication to my research.

I am very grateful to my dissertation committee members of Texas State University for reviewing my research proposal and dissertation. I want to say a big thank you to the following committee members for their time and recommendations: Dr. Christopher P. Rhodes, Dr. William T. Chittenden, Dr. Alexander Zakhidov and Dr. L. Kevin Lewis.

I also want to thank Dr. Benjamin Martin, Dr. Christopher P. Rhodes and Dr. Casey Smith as well as staff of the Analysis Research Service Centre for their assistance and training on analytical instruments and equipment at Texas State University. I also wish to extend my sincere gratitude to Dr. Josefina Arellano-Jimenez of Kleberg Advanced Microscopy Center of The University of Texas at San Antonio for training and assisting me on the atomic resolution transmission electron microscope.

I would also like to thank the following professionals for coaching and helping me with business plan and commercialization projects; Dr. Richard Phillips, George Steinke, Claudia Roeschmann, and Hauke Roeschmann.

I also wish to thank visiting researcher, Dr. El-Shazly Duraia for his assistance with characterization of nanomaterial. I also want to recognize Sibo Niu, a doctoral candidate of Texas State University for helping with fabrication and testing of lithium ion battery half cells.

I am also grateful for financial assistance from the Materials Science, Engineering and Commercialization program and the Graduate College of Texas State University. I would like to acknowledge the wonderful and talented staff of Materials Science, Engineering and Commercialization program, especially the director, Dr. Jennifer Irvin and administrative lady, Karla Pizana for their support.

Finally, I am thankful to my wife, Nari A. Banieh for her constant encouragement, and support throughout my studies. I also thank my mother, Yaa Obour for always being there for me.

TABLE OF CONTENTS

Page

LIST OF TABLES

Table **Page**

LIST OF FIGURES

Figure **Page**

ABSTRACT

Two-dimensional (2D) carbon nanosheet material graphene is the basic structure for all the different allotropes of carbon such as fullerenes (0D), carbon nanotubes (1D), and graphite (3D). Graphene is a two-dimensional (2D) layered material comprised of a hexagonal network of carbon atoms in a crystalline form. Thus, graphene is an atom thick planar sheet of sp^2 bonded carbon atoms densely packed into a honeycomb crystal lattice, the basic structure for graphite.

Graphene has risen to fame in this century due its extraordinary properties, which originates from its electronic configuration, sp^2 bonding and ability to functionalize with other elements and molecules. Graphene and its derivatives such as graphene oxide have shown promising research results for application in optical electronics, photovoltaic systems, nanocomposites, energy storage devices, and others. However, commercialization of graphene production and fabrication of graphene related products are still under investigation with a few pilot production plants.

In this doctoral research, carbon nanosheets were prepared from renewable carbonaceous materials. Specifically, carbon nanosheets were synthesized from agricultural plants such as cassava, rice and corn. The synthesis approach employed catalysts to promote gradual removal of glycosidic linkages in the renewables to form layered structures, and reducing atmosphere to remove oxygen-containing groups and retain graphitic layers. The synthesis process is cost-effective and can easily scale to produce layered carbon-based nanomaterials. The synthesized carbon nanosheets

exhibited exceptional properties such as a specific surface area of up to 2956 m^2/g and a total pore volume exceeding 5.1 mL/g.

1. LITERATURE REVIEW

1.1 Graphene – 2 Dimensional Carbon Sheet

Two-dimensional carbon nanosheet material is undoubtedly a critical raw material for emerging technologies because of its superior properties for a vast array of applications including printable electronics, catalysis, sensors, biomedical devices, and energy storage devices. Graphene is a two-dimensional (2D) layered material comprised of a hexagonal network of carbon atoms in a crystalline form [1-4]. Thus, graphene is an atom thick layer of sp^2 bonded carbon atoms, the basic structure for fullerenes (0D), carbon nanotubes (1D), and graphite (3D). Graphene has 2 atoms per unit cell, hence two sub lattices [4-9]. The extraordinary properties of graphene originates from its electronic configuration and sp^2 bonding, which results in high carrier mobility, ambipolar electric field effect, high ballistic conduction of charge carriers, high surface area, ultra-high mechanical strength, excellent thermal conductivity, high elasticity, room temperature quantum Hall effect, unexpected high absorption of white light, gas adsorption, unusual magnetic properties, charge-transfer interactions with molecules, and tunable electronic band gap [5-30].

However, graphene has to overcome several drawbacks before its full potential can be realized in practical applications. First, graphene has a linear gapless spectrum, protected by symmetry between two sublattices. A schematic of free stand-standing graphene crystal and electronic band structure (only π bands) is shown in Figure 1 [12]. Symmetry between the sublattices in graphene results in gapless spectra around K points. Therefore, graphene exhibits metallic conductivity even in the limit of nominally zero carrier concentration. This, for example, prevents the use of graphene in making

transistors. Most electronic devices rely on the presence of a gap between valence and conduction bands. Although several proposals have been made to open a gap in graphene's electronic spectra, they all require complex engineering of the graphene layer [13]. This has triggered several research works to induce and control such a gap in graphene [12-21]. It is known that a lift of this symmetry should immediately lead to a gap opening [13]. Zhou *et al.* showed that when graphene is epitaxially grown on SiC substrate, a gap of ≈0.26 eV is produced. This gap decreases as the sample thickness increases and eventually approaches zero when the number of layers exceeds four. Zhou *et al.* propose that the origin of this gap is the breaking of sublattice symmetry owing to the graphene–substrate interaction [13].

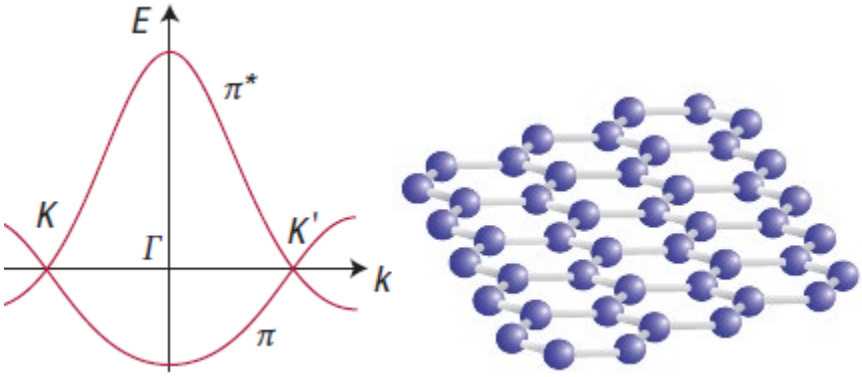

Figure 1. A schematic of free-standing graphene crystal and electronic band structure (only π-bands) [12].

Another major challenge with graphene is how to produce high quality material at commercial scale at low cost, and in a reproducible manner [31]. The quality of graphene plays a vital role as the presence of defects, grain boundaries, impurities, multiple domains, structural disorders, and wrinkles in the sheets can affect its properties.

Another concern is toxic precursors are usually used in the production of graphene, which creates hazardous wastes [31-37]. In addition, current convectional manufacturing methods for graphene are complex with high costs of production, which results in expensive graphene products. The most common techniques for the production of graphene include micromechanical cleavage, chemical vapor deposition (CVD), epitaxial growth on substrates, chemical reduction of exfoliated graphene oxide, and liquid phase exfoliation of graphite as discussed in the next section. Figure 2 shows properties of graphene and its target application(s).

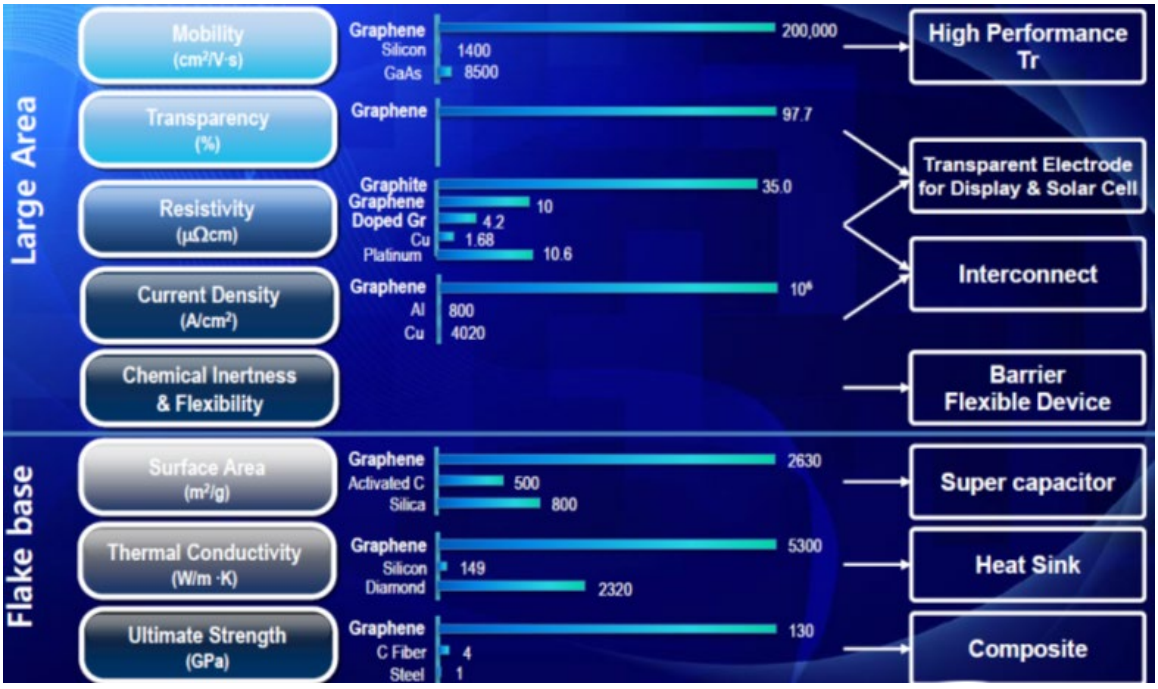

Figure 2. Properties of graphene nanomaterials and their key features, and current and future applications [32].

1.2 Syntheses of Graphene and Graphene Oxide

Currently, graphene and graphene oxide can be produced by bottom up (atom by atom growth) or top-down (exfoliation from bulk) techniques [32-39]. The use of

graphene-related materials requires large scale and cost effective production methods, providing a balance between ease of fabrication and final material quality.

1.2.1 Dry Exfoliation

Dry exfoliation is the splitting of a layered material into atomically thin sheets *via* mechanical, electrostatic, or electromagnetic forces in air, vacuum, or inert environments [5]-[8].

1.2.1.1 Mechanical Exfoliation

Crystal growers and crystallographers have been using micromechanical exfoliation (micromechanical cleavage) for decades [6]. In 2004, Novoselov *et al.* used adhesive tape to peel off single-layers of graphene sheets [14-15]. These researchers subsequently demonstrated the superior electric field effect and room temperature quantum Hall effect in exfoliated single layer graphene sheets, and received a Nobel Prize in 2010 [1], [14-15]. Micromechanical exfoliation is currently optimized to yield high quality layers. Ferrari *et al.* indicated that the size of the starting graphite limits it resulting graphene size, which is of the order of millimeters [6]. It is reported that, at room temperature, carrier mobility, μ, of as-prepared single-layer graphene measured up to 200 000 $cm^2V^{-1}s^{-1}$ [5]. Although micromechanical exfoliation is not ideal for commercial scale production of graphene, several fundamental studies and prototype devices were obtained by using micromechanical cleavage graphene of sheets [14-16].

1.2.1.2 Anodic Bonding

Anodic bonding is a common practice used to bond layers of graphene to glass films [6-8], [33]. The two key parameters for exfoliating graphene sheets in this method are temperature and voltage. Graphite is pressed on a glass substrate and a high voltage

(0.5-2 kV) is applied between it and a metal back contact. The glass substrate is heated to about 200 ^{o}C for 10-20 min [6]. Application of positive voltage to the top contact accumulates a negative charge in the glass side facing the positive electrode, which causes Na_2O impurities in the glass to decompose into Na^+ and O^{2-} ions. O^{2-} ions remain at the glass-graphite interface, inducing high electric fields and causing a single-layer of graphene to stick to the glass surface by electrostatic interaction. Temperature and voltage is used to control the number of layers of graphene sheet on a glass substrate. Figure 3 illustrates the setup for obtaining graphene sheets by using anodic bonding method. According to Ferrari *et al.* graphene flakes of up to 1 mm width have been reported by using anodic bonding [6].

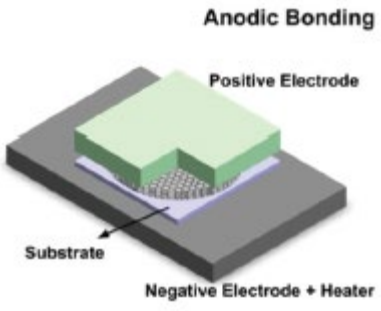

Figure 3**.** Schematic of anodic bonding [6].

1.2.1.3 Laser Ablation and Photoexfoliation

Fine control of energy density of laser beam can be used to exfoliate graphene sheets from graphite via evaporation and/or sublimation. Photoexfoliation of graphene occurs when there is no evaporation or sublimation of material and the energy of the laser beam detaches an entire sheet or part of a layer from graphite [6]. It is reported that

energy density increases with a decreasing number of layers of graphene sheet (N) up to 7 layers of graphene, and for $N > 7$, the ablation threshold saturates [50]. The authors also indicated that the number of layers of graphene sheets (N) is related to specific heat generated by the phonon scaling as $1/N$. Other researchers also prepared graphene from direct laser irradiation of graphite, successfully [51]. However, it is recommended that ablation be implemented in inert or vacuum conditions as air tends to oxidize the graphene sheets [50-51]. Although laser ablation generally produces valid results, the process requires further optimization. Moreover, this process has shown promising results even during photoexfoliation in liquid, by offering an alternate path similar to liquid phase exfoliation [52].

1.2.2 Liquid or Chemical Exfoliation

Liquid exfoliation of graphite (or any other layered material) is based on exposing the materials to a solvent with a surface tension that favors an increase in the total area of graphite crystallites [5]. The solvent is usually non-aqueous, but surfactant can be added to an aqueous solvent for liquid exfoliation [5]. The process involves three steps: 1) chemical wet dispersion of graphite in solvent; 2) exfoliation; and 3) purification (separation) of exfoliated sheets from un-exfoliated bulk flakes [6]. A related method can be utilized to prepare graphene oxide (GO) [7-10].

1.2.2.1 Liquid exfoliation of graphite

Liquid exfoliation can be done via both aqueous and non-aqueous solvents [5-6]. Ultrasonication is employed to split graphite into individual platelets. In this process, hydrodynamic shear-forces associated with formation, growth, and collapse of bubbles or voids in the liquid due to pressure fluctuation is used to control the exfoliation. After

exfoliation, the solvent-graphene interactions needs to balance the inter-sheet attractive forces [53].

Solvents that minimize the interfacial tension between the liquid and graphene flakes are best for dispersion of graphene sheets [54]. If the interfacial tension between the graphene flakes and liquid is high, the graphene sheets tend to adhere to each other, and the cohesion between them is high hindering dispersion [53-54]. Cohesion is the energy per unit area required to separate two flat surfaces [6]. Several liquids have been investigated for dispersion of graphitic materials, and liquids with surface tension, γ, of about 40 mNm^{-1} are considered best for dispersion [54]. Unfortunately, the majority of liquids with $\gamma \sim 40$ mNm^{-1} have toxic effects on organs and/or have high boiling point (>177 ^{o}C), making it difficult to remove solvent after exfoliation [6], [53-54]. Acetone, chloroform, isopropanol, and water can be used as alternative choices. However, the surface tension of water ($\gamma \sim 72$ mNm^{-1}) is too high and promotes re-aggregation of exfoliated sheets. Therefore, linear chain surfactants such as sodium deoxycholate or polymers such as pluronic may be used to stabilized exfoliates flakes by Coulomb repulsion [53].

Separation (purification) of the exfoliated sheet is achieved *via* ultracentrifugation in a uniform or density gradient medium, depending on the application of exfoliated graphene sheet. Exfoliated graphene is commonly applied as conducting inks, composites, or thin films [5]. Liquid exfoliation is a relatively cheap and easily scalable process, and does not require expensive growth on substrates. However, the exfoliation procedure and purification (separation) induce in-plane fracture [17]. Furthermore, liquid exfoliation is not well understood and requires more research to control the number of

sheets, flake thickness, and lateral sizes of graphene flakes, as well as density, viscosity, and surface tension of the resulting dispersions [33-53].

1.2.2.2 Liquid exfoliation of graphite oxide

It is important to discuss synthesis of reduced graphene oxide (rGO). This route involves oxidation of graphite in the presence of strong acids such as nitric acid or sulfuric acid. In 1859, Brodie prepared graphite oxide (GrO) by oxidizing graphite in the presence of potassium chlorate ($KClO_3$) and fuming nitric acid [55]. Following Brodie's work, Staudenmaier created a stepwise process by using sulfuric acid in one step and adding $KClO_3$ in another step to produce graphite oxide [56]. However, both methods produced a hazardous gas, chlorine dioxide, which can decompose explosively into oxygen and chlorine. Following a series of work, the first TEM image showing the presence of single sheets of graphene oxide was published in 1948 [57].

In 1958, Hummer and Offeman developed a safer process for producing graphite oxide by mixing graphite with sulfuric acid, sodium nitrate, and potassium permanganate [58]. These chemicals induce defects in the sp^2 bonded network of carbon and introduce hydroxyl or epoxide groups in the basal plane, while carbonyl, carboxylic, lactone, phenol, and quinone attach to the edges [9-10], [58]. These functional groups help dispersion in pure water, organic solvent, and aqueous mixtures with methanol, acetone, acetonitrile, 1-propanol and ethylene glycol [53]. The resulting graphite oxide flakes can be used to produce graphene oxide sheets (GO) by sonication, stirring, or thermal expansion among others [9-10]. Although the Hummer and Offeman process results in large GO flakes, up to several micrometers, this GO material is a very defective insulating nanomaterial [6]. Several reduction methods have been proposed to decrease

the oxidation states of the oxygen containing groups in order to increase its conductivity [5-10]. The commonly used reduction process is chemical treatment (by using hydrazine, hydrides, *p*-phynylene, hydroquinone, sulphur compounds, or ascorbic acid) and thermal reduction [5], [32-35]. It is reported that heat driving reduction of graphene oxide produces high quality graphene structures [6]. For example, laser heating in an oxygen-free environment can be done with a spatial resolution down to a few micrometers, and temperature up to 1000 °C, paving the way for graphene fabrication [6]. Figure 4 shows a key step in preparation of graphene oxide and reduced graphene oxide.

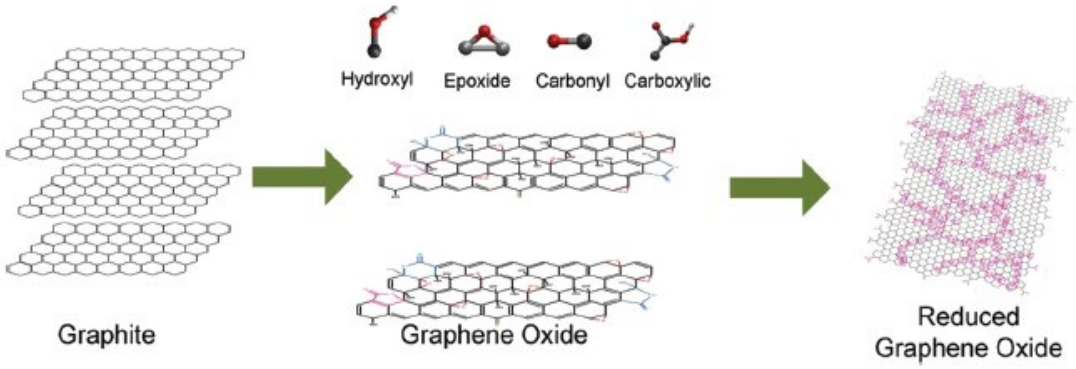

Figure 4**.** Graphene oxide preparation and reduction steps [53].

1.2.3 Growth on Silicon Carbide (SiC) and Insulating Substrates

The growth of graphene on silicon carbide (SiC) is usually called epitaxy growth, even though there is a large lattice mismatch between SiC (3.073 Å) and graphene (2.46 Å) [6]. Furthermore, the carbon rearranges itself to form a hexagonal lattice as Si evaporated from the substrate, rather than carbon deposited on the SiC surface. Generally, there are two types of epitaxial growth process depending on the substrate, homo- and hetero-epitaxy [53], [59].

In the homo-epitaxy method, the substrate is of the same composition and structure as the growing film, which minimizes defects like misfit dislocations in semiconductors. On the other hand, hetero-epitaxy growth involves growing of film on substrates with different composition and may lack perfect matching of lattices [53]. In the case of graphene, graphite is the only isostructural substrate, but it would not be very beneficial to use for growing graphene. Two potential substrates for graphene with low lattice mismatch are h-BN 1.7 % and hcp-Co 2 % [53]. The growth of layered materials on highly mismatched lattice substrates that acts as buffer layers are possible, due to their weak bonding to the substrates [5-6]. Films grown parallel to the substrate due to the anisotropic nature of their chemical bonds and the growth of graphene on SiC behaves in a similar manner [5-6].

The growth of graphene on SiC depends on the polarity of the face of the SiC crystal [33-53]. It is reported that graphene forms faster on the C-face, producing larger domains (~200 nm) of multilayered, rotationally disordered graphene, while on the Si-face, slow ultra-high vacuum annealing leads to small domains (~30-100 nm) [60-61]. The small-grain morphology was attributed to high annealing temperature. Currently, graphene growth on the Si-face has a room temperature mobility of up to 2,000 $cm^2V^{-1}s-1$, whereas the mobility measured on the C-face reached 30,000 $cm^2V^{-1}s^{-1}$ [6], [60-61]. Graphene on SiC is attractive for electronics since SiC is already established in the power electronic industry [53]. However, SiC wafers are too expensive in comparison with same size Si-wafer [5]. Furthermore, it is difficult to transfer single-layer graphene from a SiC substrate to another substrate [5-6], [53].

1.2.4 Growth on Metal by Precipitation

Deposition of carbon on metal surfaces can be achieved via flash evaporation, physical vapor deposition (PVD), chemical vapor deposition (CVD), and spin coating [53]. The choice of carbon source and substrate is a crucial part of the graphene growth on metal substrates. The carbon source can be solid (e.g. camphor), liquid (e.g. benzene) or gas (e.g. methane) [5-8], [33], [38], [43]. Generally, the type of precursor depends on what is available, cost-effective for the application, and what yields the desired films [5]. In the case of solid precursors, the solid can be vaporized, then transferred into the deposition and growth chamber or dissolved in appropriate liquid and transferred to a vaporizer. Usually carrier gas aids the transfer process.

One main selection criteria for materials for substrate is those that do not form carbide, which competes with growth of graphitic layer/graphene [5]. It is reported that carbon forms thermally stable carbides with elements such as Ti, Ta, Hf, Zr, and Si, which make them unsuitable as substrates [62]-[63]. Furthermore, each of these elements has a high lattice mismatch (> 20%) with graphene [6]. Several researchers successfully grew single-layer graphene on Ni(111), Ru(001), Ir(111), Pt(111), and Pd(100). These planes facilitate hexagonal growth of carbon atoms [5-6], [53], [64].

The growth process is achieved by exploring the high temperature solubility of carbon in interstitial sites in metals to achieve layer by layer growth up to a few atomic % [62-64]. This growth process involves annealing of the metal at high temperature (>1000 °C) in ultra-high vacuum to obtained high bulk solubility of interstitial carbon, then cooling to segregate carbon as a graphene film on the metal substrate. The growth of graphene by precipitation requires accurate control of annealing temperature, metal

thickness, annealing time, cooling rate, and metal microstructure.

In the case of CVD, several types of processes are used to obtained graphene sheets such as thermal, plasma enhanced (PECVD), cold wall, and hot wall, among others [53]. The type of CVD growth process depends on factors such as availability of precursor, cost, material quality, thickness, and structure needed for the specific application. Generally, CVD graphene is grown on thin metal films while the CVD process for carbon nanotubes utilizes growth on metal nanoparticles [5], [33], [64].

The first report of CVD growth of uniform larger area (cm^2) graphene was on polycrystalline Cu foils [5-6]. The large area growth was attributed to low solubility of C in Cu, and partial catalytic activity of Cu during the CVD process [6]. At present, the process is expensive due to large energy consumption, and removal of metal layer/substrate. Despite this complex transfer process, Bae *et al.* grew graphene film on Cu foil (30 inches) that has a carrier mobility of $\sim 7350\ cm^2V^{-1}s^{-1}$ at 6 K [65].

One main challenge with most metal substrates is the difference in thermal expansion between graphene and most metals, which results in significant wrinkles upon cooling. Furthermore, surface roughening and sublimation of some metals (e.g. Cu) at high growth temperatures (> 1000 °C), also impedes the quality of graphene sheets. This has led to exploration of metal alloys as suitable substrates for CVD graphene growth [36]. Despite the presence of defects, grain boundaries, inclusions of thicker layers, and so on, such films are ready for use in transparent conductive coating applications such as touch screens [5].

1.3 Characterization

Characterization techniques typically employed in graphene research include but are not limited to Raman spectroscopy, X-ray diffraction (XRD), transmission electron microscopy (TEM), and scanning electron microscopy (SEM) coupled with electron dispersive X-ray spectroscopy (EDX).

1.3.1 Raman Spectroscopy

Raman spectroscopy is a standard nondestructive tool for characterization of various carbon materials [46]-[48]. Carbon materials possess their identity and physical properties on the ratio of sp^2 (graphite-like) to sp^3 (diamond-like) bonds [46-49]. There are many forms of sp^2-bonded carbons with varying degrees of graphitic ordering, ranging from microcrystalline graphite to glassy carbon. Typically, amorphous carbon has a mixture of sp^3, sp^2 and even sp^1 sites with the presence of up to 60 at. % hydrogen [48]. Figure 5 shows a ternary phase diagram for carbon materials; where a-C means amoprhous carbon; a-C:H is hydrogenated amorphous carbons with small C-C sp^3 content; ta-C is tetrahedral amorphous carbon with higher sp^3 content; and its hydrogenated analog is ta-C:H.

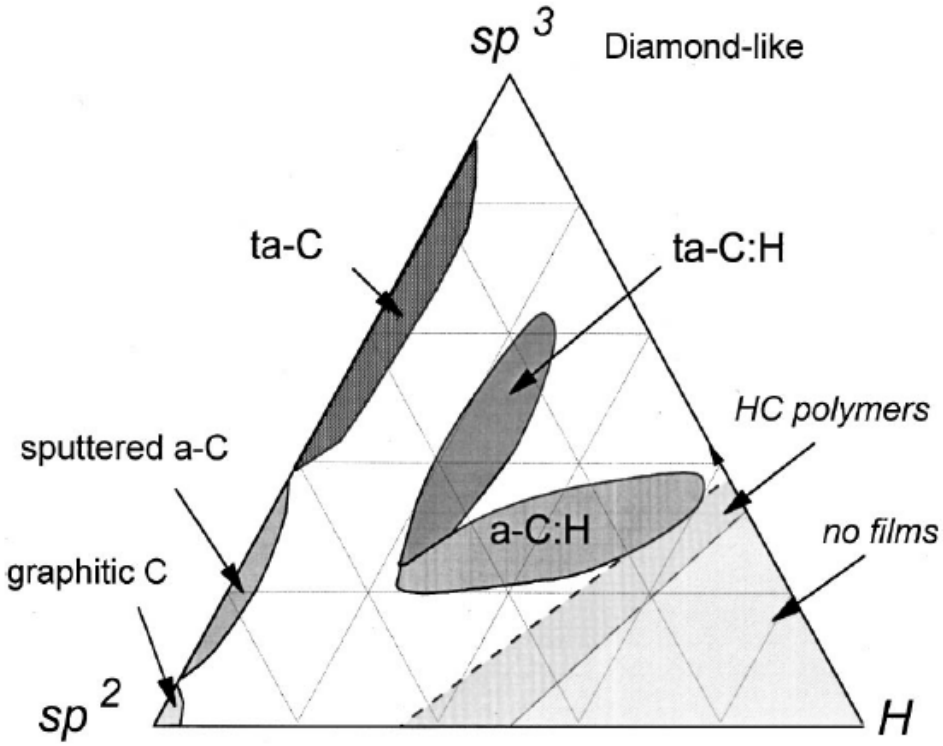

Figure 5**.** Phase diagram of carbon materials, where three corners correspond to diamond, graphite and hydrocarbons [48].

A Stokes phonon energy shift caused by laser excitation creates two main Raman peaks in graphitic sheets: G, and G' (2D) bands are observed around 1580, and 2700 cm^{-1}, respectively [46]. The motions of carbon in the G and D modes are shown in Figure 6, [48]. The G-band corresponds to tangential stretching mode (E_{2g}) (doubly degenerate zone center) of highly oriented graphitic material [47]. Its eigenvector involves the in-plane bond-stretching motion of pairs of carbon sp^2 atoms and does not require the presence of six fold rings and therefore occurs at all sp^2 sites, in aromatic and olefinic molecules [48]. The D-band is a breathing mode of A_{1g} symmetry involving phonons near the *K* zone boundary. That is D-band originates from first order boundary phonons. The

presence of the D-band is a characteristic of lattice distortion in graphene sheets and its intensity is strictly connected to the presence of sixfold aromatic rings [48]. The second order boundary phonons appear as 2D-bands during Raman scattering [46]. D and 2D peak positions are dispersive (change with laser excitation energy). The Raman spectra of high quality pristine graphene shows no D-band, which indicates the absence of defect in the materials due to its crystal symmetry. In order for a D-band to appear, a charge carrier must be excited and inelastically scattered by a phonon, then a second elastic scattering by a defect or zone boundary must occur to results in recombination [46]. D-band appear at ~ 1350 cm^{-1} in defected graphite with 514 nm laser excitation energy.

On the contrary, 2D-band always occur because the second scattering (either on the initially scattered electron/hole or its complementary hole/electron) in the process is also inelastic scattering from a second phonon [46]. For this reason, a sharp D-band is observed for single-layer graphene edge, whereas 2 peaks appears in bulk graphite edge as shown in Figure 7 [47]. As expected, no D peaks are observed in centers of single layer graphene and bulk graphite (Figure 8). In pristine graphene, the G-band is observed at 1580 cm^{-1}. In addition, Raman spectroscopy can differentiate between the numbers of layers of pristine graphene by comparing the intensity of the G-band. The number of layers increases with increasing intensity of the G-band [47], [66].

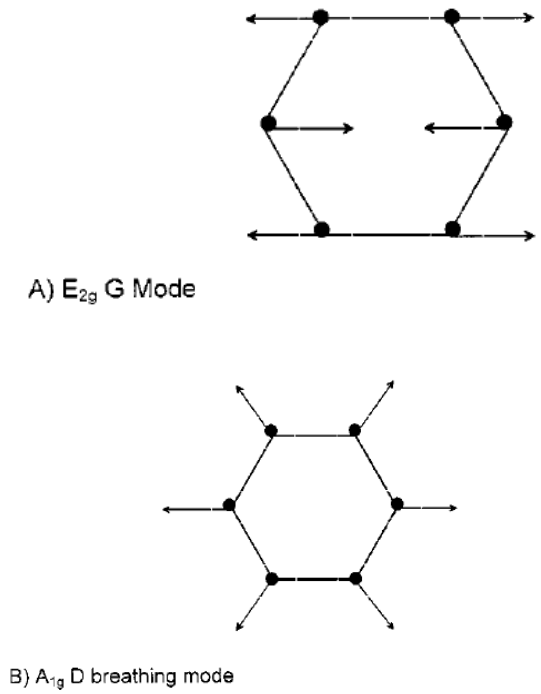

Figure 6**.** Carbon motion in D and G modes [48].

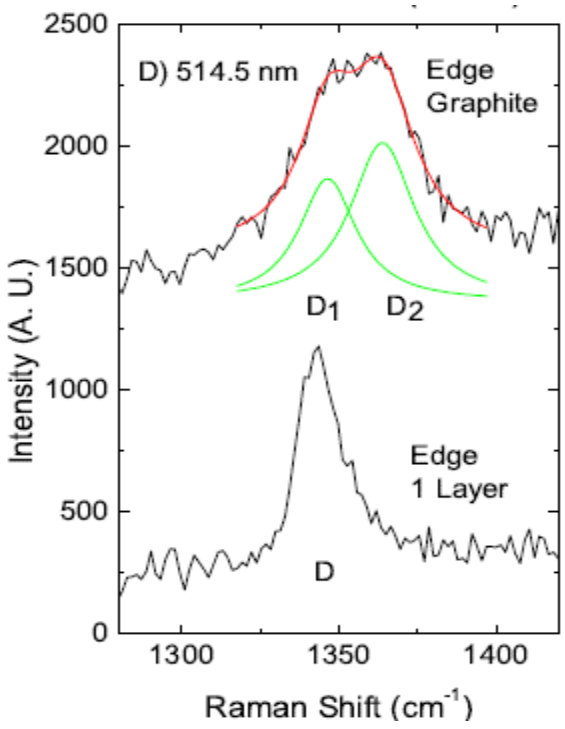

Figure 7**.** D band in graphene edge and graphite edge, [47], [66].

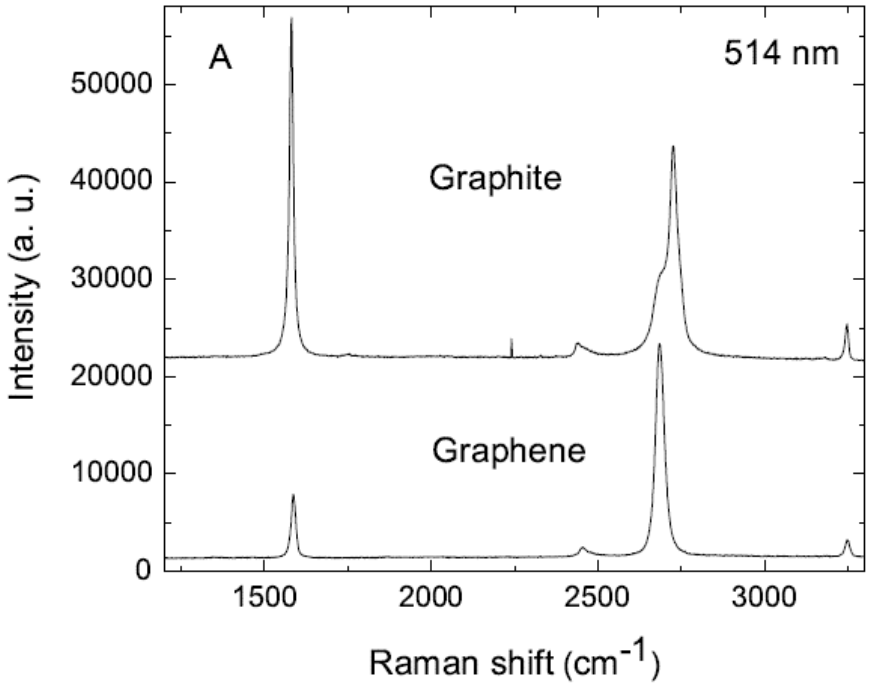

Figure 8**.** Comparison of Raman spectra at 514 nm for bulk graphite center and single layer graphene center, [47]. Scaled to have similar height of 2D peaks.

Furthermore, the ratio of intensity of the D-band (I_D) to G-band (I_G) indicates the level of disorder in graphene [46-48]. When the disorder increases, I_D/I_G, shows two different regimes; low defect density and high defect density. In the low defect density region, I_D/I_G increases with increasing defect density due to creation of more elastic scattering. This regime results in nanocrystalline graphite and occurs up to a regime of high defect density, where I_D/I_G will begin to decrease, as increasing defect density results in a more amorphous carbon structure [46-48]. Typically for amorphous carbon, the intensity of the D peak is lower than the G peak and the widths of the peaks are also very broad. Figure 9 shows that increasing the concentration of sp^3 content decreases I_D/I_G , but increases the intensity of G-band peak position in Raman spectra.

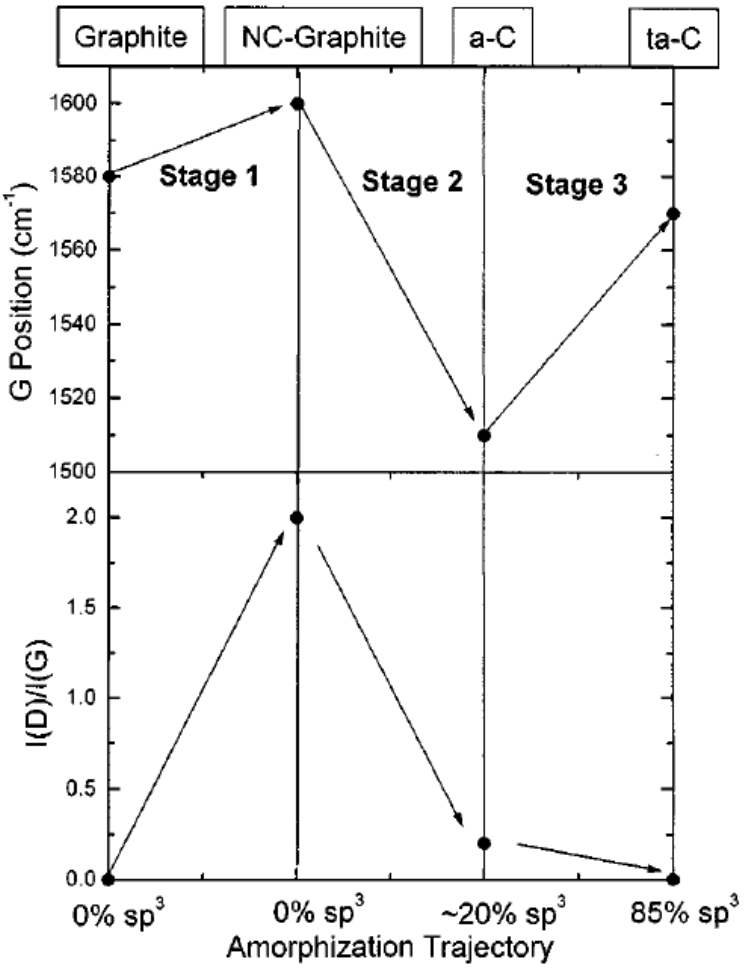

Figure 9**.** Amorphous carbon trajectory from graphite, showing variation of the G position and intensity ratio of D peak to G peak. Where NC is nanocrystalline graphite, a-C is amorphous carbon, and ta-C is tetrahedral amorphous carbon, [47].

1.3.2 X-ray Diffraction

X-ray diffraction (XRD) is a commonly used technique to identify most crystalline phases in materials. Although, XRD is a not perfect for determining the number of layers of graphene sheets, it can positively identify the basal reflection of the (002) plane in pristine graphite at two-theta of 26.6º in XRD pattern. The (002) plane

originates from local periodic turbostratically stacked defective graphene layers, whereas the (100) plane is associated with the lateral arrangement of the carbon atoms within each layer [67]. A reduction in the intensity of the (002) plane indicates that the sample is predominantly composed of exfoliated single carbon sheets. Furthermore, a shift of the (002) to lower diffraction angles means the average distance between graphene sheets are longer than graphite. This peak shifts to a lower angle ~ 2θ =13.9º, when pristine graphite is strongly oxidized to graphite oxide [5-6]. It is reported that after thermal exfoliation and reduction of graphite oxide, this diffraction peak is almost removed in the resulting graphene nanosheets [33]. Furthermore, a reduced plane (100) intensity is due to lateral disordering of carbon atoms in the graphene layers [67].

1.3.3 Transmission Electron Microscopy

High resolution transmission electron microscope (HR-TEM) can determine the thickness of graphene sheets with high precision and accuracy by measuring the thickness of a large number of images and taking the statistical mean [33]. Furthermore, analysis of foldings at the edges or within the free standing sheets gives the number of layers by direct visualization, since at a folding the sheet is locally parallel to the beam [47]. A more accurate way of identifying the number of layers of graphene is by electron diffraction patterns. This technique involves changing the incidence angles and their corresponding electron diffraction [33], [47]. Ferrari *et al.* showed that electron diffraction pattern of bi-layer shows A-B staked with intensity of the {11-20} diffraction spots (outer hexagon) roughly twice that of the intensity of {1-100} spots (inner hexagon) in single layer graphene [47]. This data also confirmed that multi-layer graphene has the same stacking as graphite. Figure 10 shows electron diffraction pattern of bi-layer and

single-layer graphene and their intensity profiles obtained using HR-TEM [47].

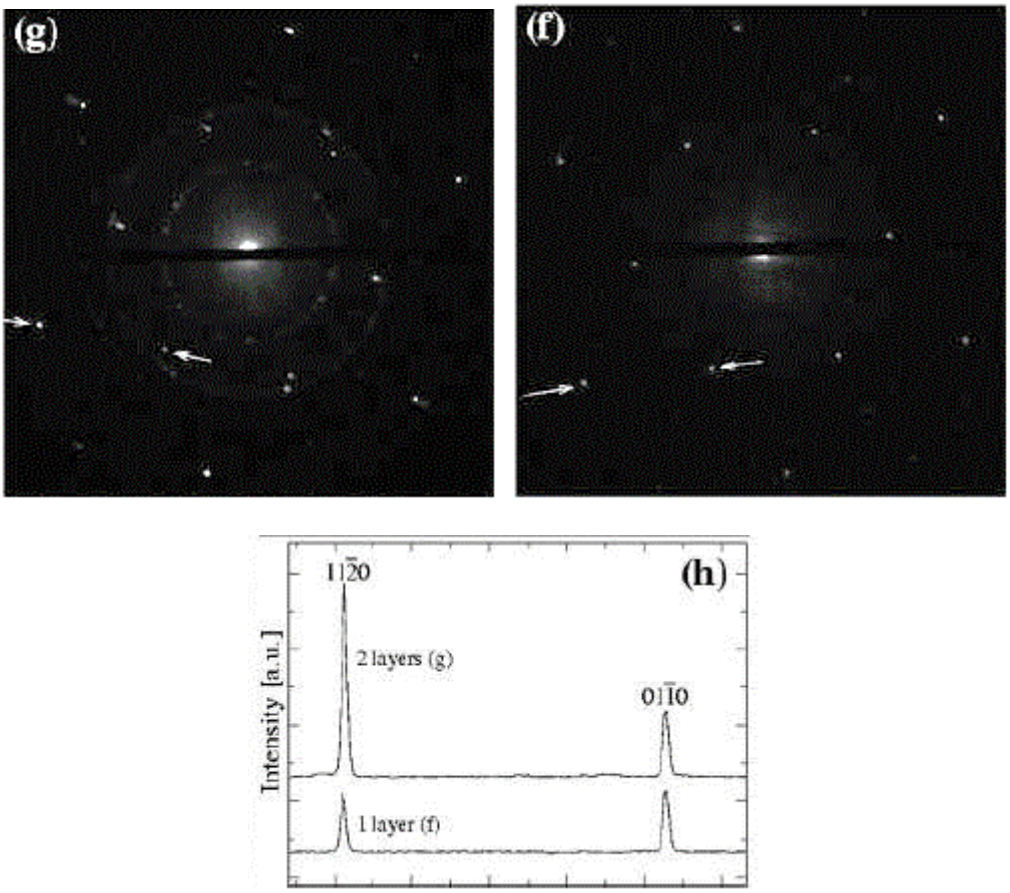

Figure 10**.** Electron diffraction profile of intensity along the arrows in (f) single-layer graphene and (g) bi-layer graphene, [47].

1.3.4 Scanning Electron Microscopy

In general, scanning electron microscopy (SEM) is a technique for analyzing the morphology, topography, and composition of nanomaterials. SEM images of graphene usually provide detailed information about the topography and morphology. Moreover, when SEM is coupled with electron dispersive X-ray spectroscopy (EDS), the amount of

oxygen and other impurities in graphene or graphene oxide sheets can be determined based on their elemental compositions in atomic weight fractions.

2. PURPOSE AND SCOPE

2.1 Gap in Research

It is worthwhile to point out that although several methods for preparing carbon nanosheets are reported in the literature, none of them offer cost effective and ecofriendly way of producing high surface area and pore volume carbon nanosheets at scale for potential application in energy storage devices.

Currently, almost all graphene researchers are focused on trying to prepare graphene sheets from graphite using processes developed in the late 1940s, popularly called Hummer's and Staudenmaier methods. Graphite is the most thermodynamically stable form of carbon, and for this reason, single layer graphene sheets tend to stack together as nano-graphite after preparation using Hummer's and Staudenmaier methods. This re-stacking of graphene sheets results in nano-graphite product with low surface area typically below 1000 m^2/g , although the theoretical surface area of single layer graphene is more than 2632 m^2/g. Beall *et al.* reported formation of graphitic layers (graphene sheets) from coal and humic acid via a hydrothermal method [68-69]. Although the Beall *et al.* method completely eliminated graphite as the starting carbon source, the resulting graphene product had a low surface area and poor electrical conductivity.

The overall goal of this doctoral research was to develop a process for producing carbon nanosheets with exceptional properties from a renewable feedstock in an extremely cost effective way that may lead to industrial scale production. It was hypothesized that carbon nanosheets can be prepared from a sustainable feedstock by using a green synthesis approach. In this contribution, the hypothesis was validated and confirmed scientifically. Graphitic sheets were prepared from a renewable carbonaceous

material by applying the right thermochemical conditions. The synthesis process employed is cost effective and the resulting graphitic carbon nanosheets possess superior properties when compared with previous methods discussed in Chapter 1.

3. EXPERIMENTAL

3.1 Raw Materials

Pure ethylene glycol, ethanol, phosphoric acid, phosphorous acid, hydrochloric acid, and cassava extract were used as precursors in the preparation of carbon nanosheet. Ethylene glycol, and ethanol were supplied by Alfa Aesar. Phosphoric acid solution and phosphorous acid crystals were purchased from Sigma Aldrich Co. The cassava extract, popularly called Gari, was obtained from a local African market in Austin, Texas. The precursors used in this research are summarized in Table 1.

Table 1. Summary of precursors.

Chemical	Molecular Formula	Purity
Ethylene glycol	CH_2OHCH_2OH	99.9 wt %
Ethanol	CH_3CH_2OH	≥ 99.5 wt %
Phosphoric acid solution	H_3PO_4	≥ 85 wt %
Phosphorous acid	H_3PO_3	≥ 99.0 wt %
Hydrochloric acid	HCl	≥ 37 %

3.2 Preparation

A total of 4.0 g of cassava extract was placed in a 50 mL Pyrex glass beaker. 2.0 g of phosphorous acid was dissolved in 4 mL of deionized water and added to the cassava extract. The mixture was stirred thoroughly and exposed to 100 ^oC for 24 h in a convection oven. After heating, the sample was subjected to rapid and uniform heating for 10 min by using microwave irradiation (1000 W). The final solid product after microwave heating was washed thoroughly in deionized water and sometimes (10 %

HCl) to remove any unreacted precursors and followed by drying in an oven at 100 ^{o}C overnight. Additional batches were prepared by using the above preparation route by varying the concentration of phosphorous acid or phosphoric acid to cassava extract from 5 wt. % to 75 wt. %.

3.3 Thermochemical Treatment

The washed and dried sample was further treated in a tube furnace to remove oxygen containing groups from the sample. The pretreated sample was put in a porcelain or quartz combustion boat and placed inside a quartz tube for thermochemical treatment. The reactor was connected with two mass flow meter/controller (Alborg mass flow controllers) to monitor and control the flow rates of H_2 and Ar gases. All the mass flow controllers were turned on for 30 min to warm up and reach equilibrium temperature before flowing gases. The sample was ramped at 15 ^{o}C/min from 20 ^{o}C to 1000 ^{o}C and held at 1000 ^{o}C for 1 h. The thermal treatment was carried out in a gas mixture containing 50 vol. % argon and 50 vol. % hydrogen gas, flowing at a total rate of 100 mL/min. A typical sample size of 2 g was exposed to thermochemical treatment in the quartz reactor.

3.4 Structural Analysis

X-ray powder diffraction (XRD) is a versatile non-destructive analytical technique primarily used for phase identification of a crystalline material and can provide information on unit cell dimensions. The results of an XRD measurement show phases present (peak positions), phase concentrations (peak heights), and crystallite size (peak width). Conversion of the diffraction peaks to d-spacings allows identification of the crystalline material because each phase has a set of unique d-spacings. Typically, this is achieved by comparison of d-spacings with standard reference patterns. In addition,

average crystallite sizes of the synthesized materials can be estimated using Scherer's equation. Structural characterization of samples was analyzed by Rigaku SmartLab X-ray diffractometer using Cu $K_{\alpha 1}$ X-ray. XRD characterizations were conducted under conditions of room temperature and atmospheric pressure. Samples were scanned from 2θ of 3 º to 70 º at scan speed of 4.1008 º /min and step width of 0.0100 º. The diffractometer generated Cu Kα1 X-ray at operating power of 40 kV and 44 mA with 1.0 mm incident slit.

3.5 Morphological Analysis

Scanning electron microscopy (SEM) is a type of electron microscopy that images the sample surface by scanning it with a high-energy beam of electrons in a raster scan pattern. The electrons interact with the atoms that make up the sample producing signals that contain information about the sample's surface topography, composition and other properties such as electrical conductivity. Samples were imaged using a FEI Helios NanoLab 400 Dual Beam system, which is a fully digital Field Emission Scanning Electron Microscope (FE SEM) equipped with Focused Ion Beam (FIB) technology. The NanoLab 400 Dual Beam system was coupled to Texture and Elemental Analytical Microscopy (TEAM) – Energy Dispersive X-ray spectroscopy (EDAX) for elemental analyses. SEM images and EDX spectra of the carbon based materials were placed on double sided copper tape. SEM images were obtained by scanning samples at 15 kV and 0.34 nA in immersion mode.

3.6 Other Analytical Instruments

A surface area analyzer was used to measure the specific surface area, pore size, and pore volume of the carbon nanosheet powder samples. In physical gas adsorption, an

inert gas, usually nitrogen is adsorbed on the surface of a solid material. This occurs on the outer surface and, in the case of porous materials, also on the surface of pores. Adsorption of nitrogen at a temperature of 77 K leads to a so-called adsorption isotherm. High-quality surface area, and porosity data was obtained by applying varies models to chemisorption and physisorption isotherm data. The Micromeritics ASAP 2020 software was used to collect isotherm data for various analyses such as BET surface area, Langmuir surface area, t-plot, total pore volume, BJH adsorption and desorption, MP-Method, and DFT pore size and surface energy. Details of the above models is reported in Appendix A, [71-77]. The Micromeritics ASAP 2020 Surface Area & Porosity Analyzer was utilized to measure adsorption and desorption isotherms of prepared samples using nitrogen gas. A typical sample size was about 100 mg and degassed at 160 ^{o}C for 16 h under 5 mm Hg vacuum before isotherm measurements.

Transmission electron microscopy (TEM) is a technique whereby a beam of electrons is transmitted through an ultra-thin specimen, interacting with the specimen as it passes through. TEMs has a significantly higher resolution than light microscopes, owing to the small de Broglie wavelength of electrons. The Kleberg Advanced Microscopy Center at The University of Texas at San Antonio provided the service for external TEM characterization of synthesized samples. The atomic resolution imaging, electron diffraction, and electron energy-loss spectroscopy (EELS) analyses were conducted by utilizing an aberration-corrected microscope on the STEM mode JEOL ARM 200F with a spatial resolution of 78 picometers.

Raman scattering is a two-photon event, commonly used to obtain information about the structure and properties of a molecules from their vibrational transitions.

Raman radiation is observed as a shift in frequency, hence energy, as a result of vibrational energy that is gained or lost in molecule, between incoming radiation that creates an induced dipole moment, and the radiation emitted by this induced dipole. Horiba LabRAM HR Evolution was used to obtain Raman spectra of prepared samples. The Horiba LabRAM HR Evolution was equipped with three excitation lasers (532nm, 633nm, 785nm), motorized XYZ stage for optical mapping and has high spectral resolution (<0.5 cm^{-1}). In addition, functional groups in prepared samples were revealed by utilizing broadband IR radiation from Bruker ALPHA II FTIR Spectrometer to probe the vibrational modes of molecule in the samples. Attenuated Total Reflectance (ATR) sampling module with diamond/germanium window was used to acquire IR spectra of prepared samples.

X-ray Photoelectron Spectroscopy (XPS) also referred to as Electron Spectroscopy for Chemical Analysis (ESCA) was performed on the prepared samples. XPS is an elemental analysis technique which is capable of detecting all elements except for H and He and has a nominal detection limit of ~ 0.1 at %. Soft X-ray radiation is directed at the sample to induce emission of inner shell electrons. Measuring the characteristic kinetic energy of the emitted electrons is used to determine their binding energy and therefore what atom they came from as well as the local bonding scheme. Samples were measured at a 90° Take-Off-Angle (TOA) yielding a sampling depth of ~10 nm. The analysis area was ~500 μm in diameter. Analyses were performed with a monochromatic Al kα X-ray source. Charge neutralization of the sample surface was achieved with the use of a low energy electron flood gun. Energy scales of the spectra are referenced to the carbon 1s C-C/C=C/C-H signal at 284.5 eV. High-energy resolution

(hi-res) XPS analyses of the carbon 1s, phosphorus 2p and oxygen 1s regions were also performed on the prepared sample. XPS hi-res analysis provides information on the bonding state (chemical environment) of the element in question. The interpretation of the data is based on literature references and is empirical. Hi-res of the C region of graphite presents mostly C=C with about 6.5 % content Pi-Pi* transition.

TA Instrument thermogravimetric analyzer (TGA) model Q50 was used to measure the weight loss associated with samples during thermal treatment. TGA principal uses include measurement of a material's thermal stability and composition. About 50.0 g of phosphorous acid was dissolved in a 300 mL deionized water. A total of 100 g of cassava extract was added to the solution and stirred thoroughly. The mixture was exposed to 100 ^{o}C for 24 h in a convection oven in air atmosphere to form intermediate mixture. This intermediate materials analyzed using a TA Instrument TGA (Q50). The intermediate sample was ramped at 10 ^{o}C/min from 25 ^{o}C to 1000 ^{o}C in argon purge gas flowing at 40 mL/min. Figures 11 and 12 show weight loss curves of raw cassava extract and cassava treated with 33.3 % H_3PO_3, respectively. It was observed that cassava treated with 33.3 % H_3PO_3 exhibited relatively lower weight loss of 55 % below 550 ^{o}C, while raw cassava lost almost 85 % at the same temperature. However, the acid treated sample underwent a second weight change event onset at about 700 ^{o}C, which resulted in a carbon nanosheet residue of about 8.9 %.

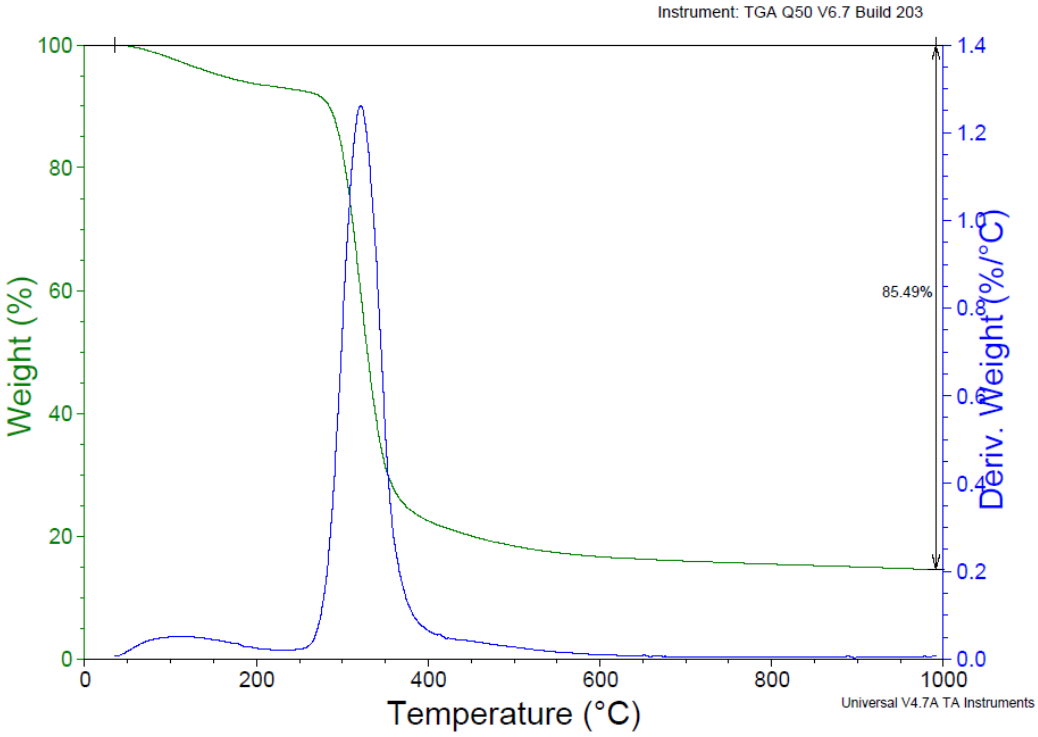

Figure 11. TG curves of raw cassava extract.

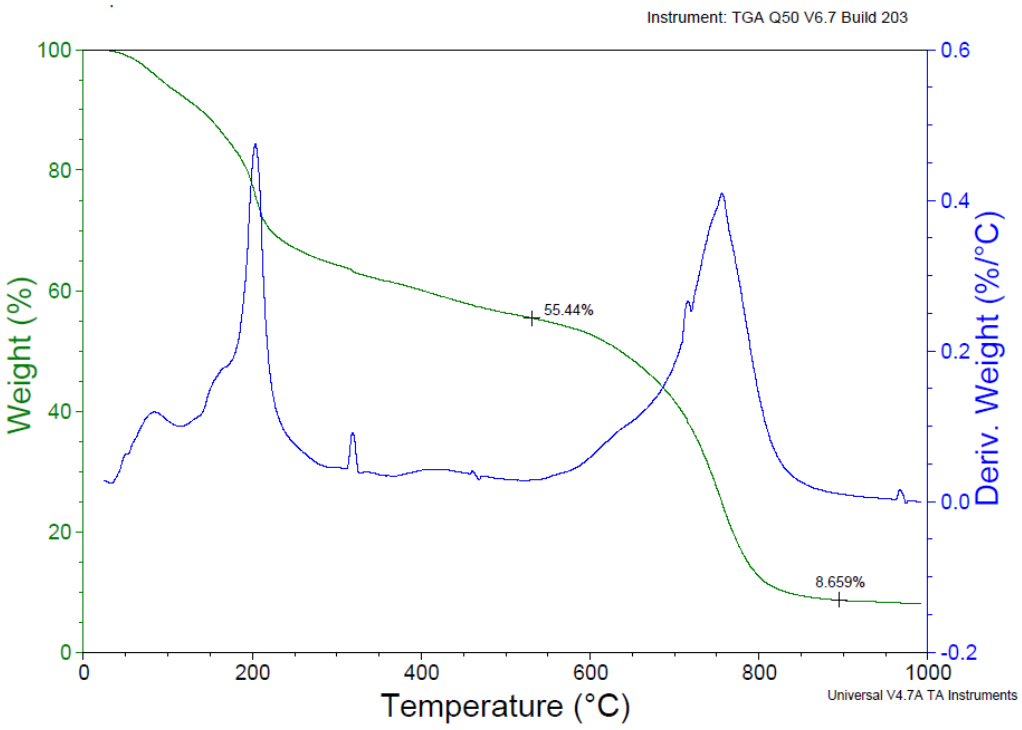

Figure 12. TG curves of raw cassava extract treated with 33.3 % H_3PO_3.

In another experiment, a total of 60 g of cassava extract was added to 200 mL of phosphoric acid and stirred thoroughly. The mixture was exposed to 160 ºC for 3 h in a convection oven in air atmosphere to form intermediate mixture. About 10 mg of intermediate sample was thermally analyzed in TA Instrument Thermogravimetric Analyzer (model Q50). Figure 13 shows the TG curves obtained when the sample was ramped at 10 ºC/min from 25 ºC to 1000 ºC in argon gas flowing at 40 mL/min. The TG curves shows the sample undergoes an initial weight loss of ~ 17 % at 200 ºC, subsequently followed by a second weight loss at 300 ºC. The first two events were attributed to loss of water and evaporation of excess H_3PO_4 in the samples. Another evolution of gases is observed at about 495 ºC, before the onset of a major weight change event at 737 ºC. About 58 % of the sample weight is lost, leaving only 6.5 % material in the crucible at 1000 ºC.

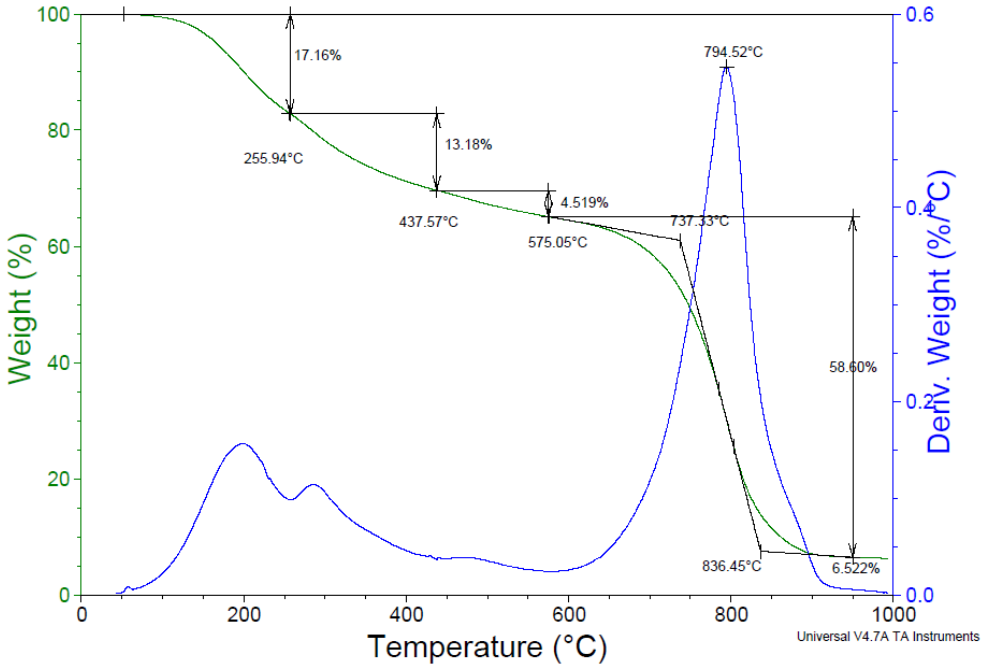

Figure 13. TGA curves of intermediate sample obtained from acid treated cassava extract 81 % H_3PO_4.

4. RESULTS AND DISCUSSION

4.1 Overview

In this doctoral research, it was hypothesized that graphitic carbon nanosheets can be prepared from a plant feedstock by applying the right thermochemical conditions. This hypothesis was based on how natural graphitic layers are formed from coal seams. It is well known that coal and peat are formed from plant remains and other organic matter buried in the earth's crust [78]. In addition, there is evidence of graphite formation from metamorphism of coal seam under high pressure and high temperature in earth crust typically under inert conditions [79].

For the purpose of this discussion, coal originates by geologic forces acting on peat, and when metamorphosed sufficiently coal becomes graphite [78]. However, not all graphite is derived from coal. Graphite is the most stable form of carbon under standard conditions. In addition, graphite can be produced from various types of carbonaceous material artificially.

Peat is an unconsolidated, hydrophilic, carbonaceous sediment, formed by accumulation of partially fragmented and decomposed, more or less altered, and commonly heterogeneous plant remains, which retains more than 75 per cent of moisture and less than 12 per cent mineral matter in saturated natural deposits [78]. Peat is formed in wet conditions where excess water obstructs flows of oxygen from the atmosphere, slowing rates of decomposition and thereby the peat deposits are protected from dissipation by persistent moisture relationships in certain geologic situations. Schopf defined coal as a readily combustible rock containing more than 50 per cent by weight

and more than 70 per cent by volume of carbonaceous material, formed from compaction or induration of variously altered plant remains similar to those of peaty deposits [78].

Therefore, it can be considered that coal originates by transformation of peat and, by metamorphic alteration, terminating in an equivalent manner by formation of the highest grade of coal called graphite.

In order to validate and confirm the hypothesis of transforming plants to graphitic nanosheets scientifically, first acid catalysts that can dehydrate renewable carbonaceous material in wet conditions were explored. Renewable feedstocks such cassava extract, rice and corn were selected because of their high carbon content in the form of amylose and amylopectin. The structure of amylose $(C_6H_{10}O_5)_n$ and amylopectin, branched $(C_6H_{10}O_5)_n$ are well known and shown in Figure 14. Phosphorous acid and phosphoric acid were used as catalysts to dehydrate renewable carbonaceous materials by removing glycosidic bonds in the amylose and amylopectin to form more double carbon-carbon bonds and cyclic carbon-carbon network. This step is critical for formation of intermediate carbon-based material which contains a limited amount of hydroxyl, carboxylic, carbonyl, alkoxy and epoxy groups.

Second, the resulting intermediate products from acid treated plants were exposed to elevated temperatures in a reducing atmosphere to remove oxygen-containing groups and other volatiles in the materials and thereby aid formation of graphitic nanosheets. Similar approaches have been used by other researchers to reduce graphene oxides [33-35]. This final step activates the intermediate carbon-based material to initiate chemical bonding of carbon atoms to form hexagonal planar network of mainly sp^2 hybridization. This occurs by at least removing oxygen atom and releasing hydroxyl portion of the

intermediate carbon-based material to result in a fused aromatic ring structure within the sheet is retained and other groups or molecules are released. Figure 15 depicts hypothetical mechanism for removal of water from glucose unit and formation of aromatic carbon structure.

In this experimental discussion, the effect of the presence of phosphorous acid and phosphoric acid on the thermochemical reaction of cassava extract to form carbon nanosheets were studied. Specifically, attempts were made to form thin sheets of carbon-based materials by varying the wt. % of H_3PO_3 from 33.3 % - 50 % in balance of cassava extract; wt. % is based only on H_3PO_3 and cassava extract and does not include the solution/solvent water. In the second part, the H_3PO_3 was replaced by H_3PO_4 and the concentrations were varied with respect to cassava extract. The results showed the formation of carbon nanostructures with sheet-like morphologies with extremely high surface areas up to 2956 m^2/g and large total pore volume exceeding 5 mL/g.

In addition, the experimental data revealed formation of carbon nanosheet structures formed from cassava, rice and corn in the absence of acid catalysts. Micrograph images revealed the catalyst-free synthesis routes resulted in formation of wrapped-graphene structures and buckyball like nanostructures.

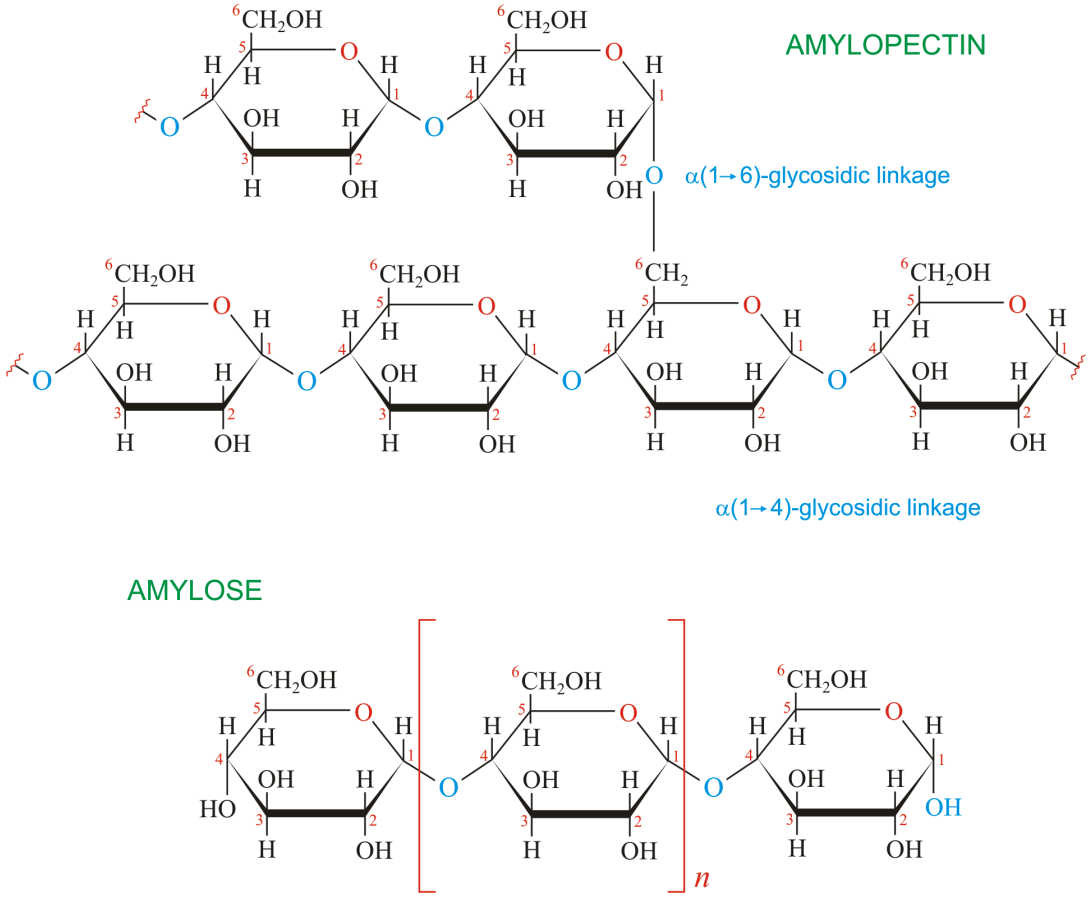

Figure 14. Idealized structure of amylose and amylopectin [80].

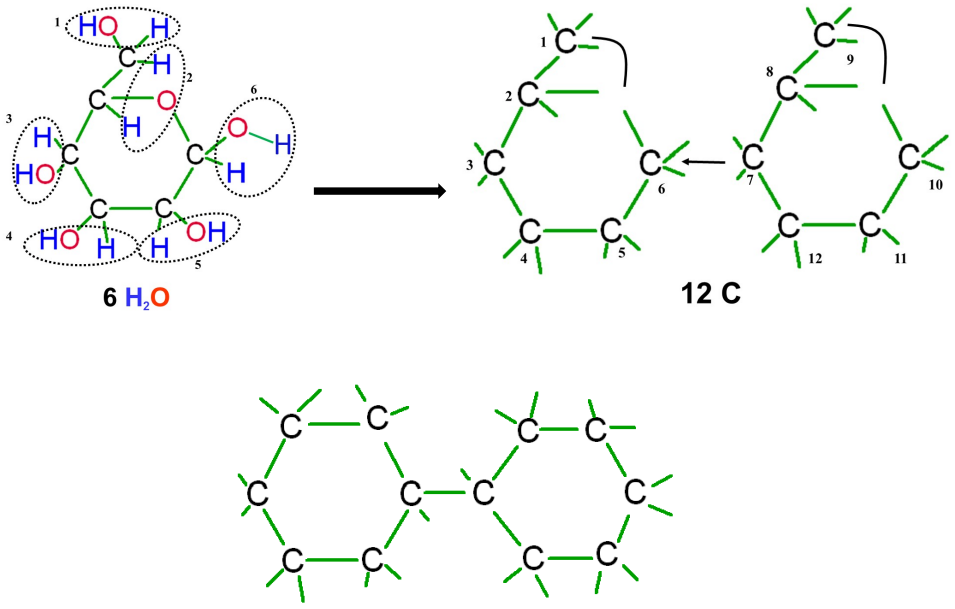

Figure 15**.** Hypothetical mechanism for hexagonal arrangement of carbon.

4.2 Characterization Cassava extract and H_3PO_3

The X-ray powder diffraction (XRD) pattern of raw cassava extract (without any acid) was exposed to 1000 ^{o}C under a hydrogen atmosphere is shown in Figure 16. The pattern shows two peaks at 2**θ** of 24.36 ^{o}, and 44.54 ^{o} that correspond to crystallographic plane (002) and (101) of graphitic material, respectively.

The XRD pattern of raw cassava extract showed mainly broad peaks typical of short-range ordered carbon materials. Elemental analysis data of raw cassava shows it contains about 85.9 at. % of carbon and 14.1 at. % oxygen as displayed in Figure 17 and Table 2.

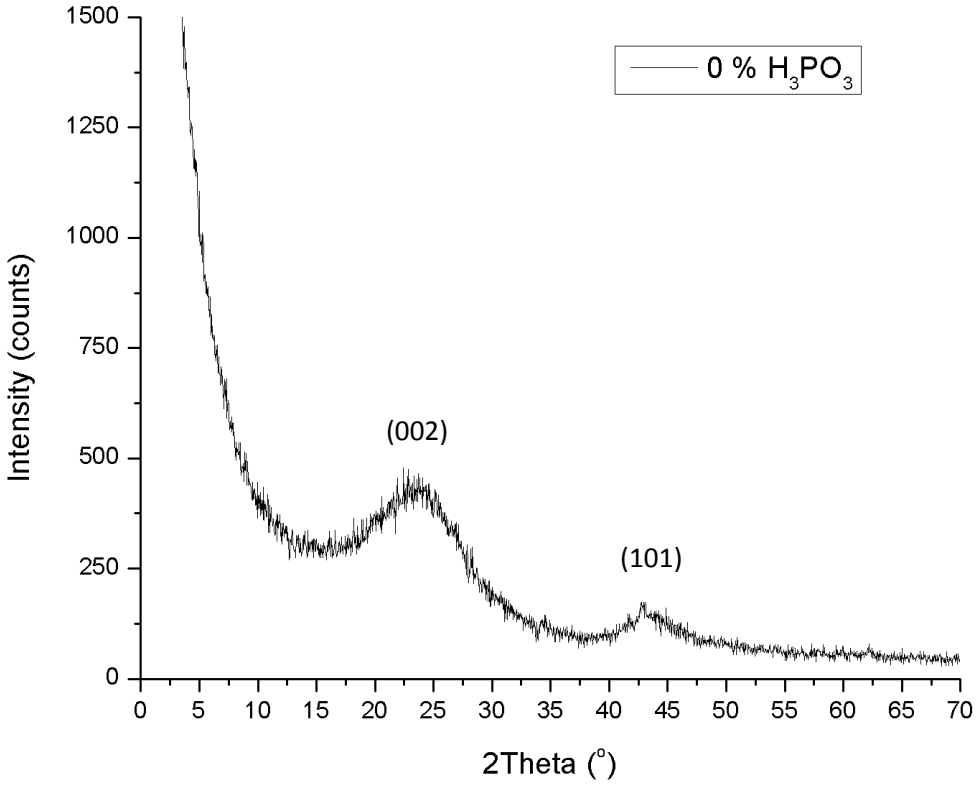

Figure 16. XRD of cassava root exposed to 1000 °C under a hydrogen atmosphere.

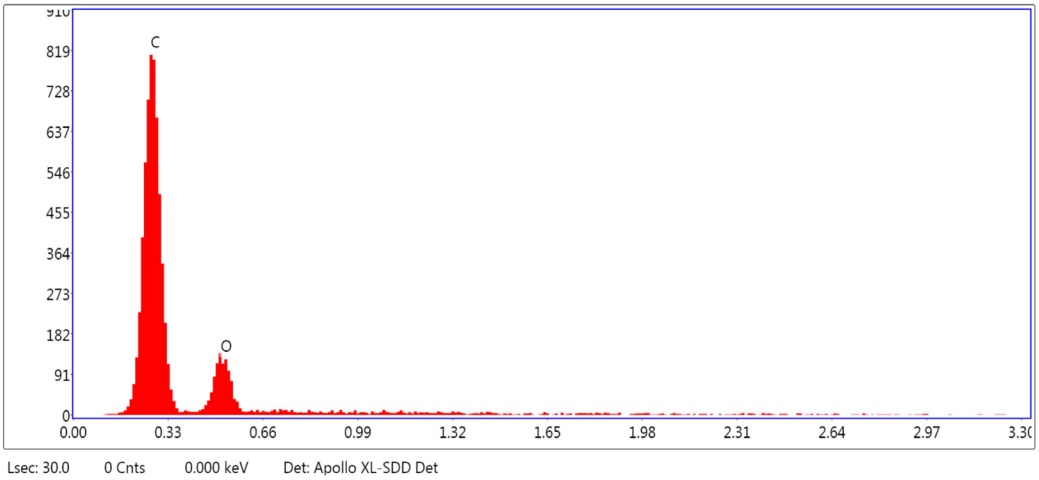

Figure 17. EDX spectrum of raw cassava extract.

Table 2. Elemental composition of raw cassava extract.

Wt. % H_3PO_3	Temperature (°C)	C (at. %)	O (at. %)	P (at. %)
0	25 °C	85.91	14.09	-
33.3	Exposed to 100 °C	57.57	36.17	6.26
33.3	Exposed to 500 °C	25.19	49.03	25.78
33.3	Pretreated at 100 °C followed by Microwave synthesis	89.35	9.35	1.30
33.3	Heat treated at 1000 °C after microwave synthesis	96.04	3.69	0.27

The XRD pattern of the intermediate material displayed a broad peak, although scanning electron micrograph images revealed a sheet-like structure fused together as shown in Figure 18. EDX spectrum indicated this fused sheet-like structures composed of about 36.2 at. % phosphorus, 57.6 at. % carbon and 6.2 at. % oxygen. Table 3 and Figure 19 present elemental compositions data of cassava extract pretreated with 33.3 wt. % H_3PO_3.

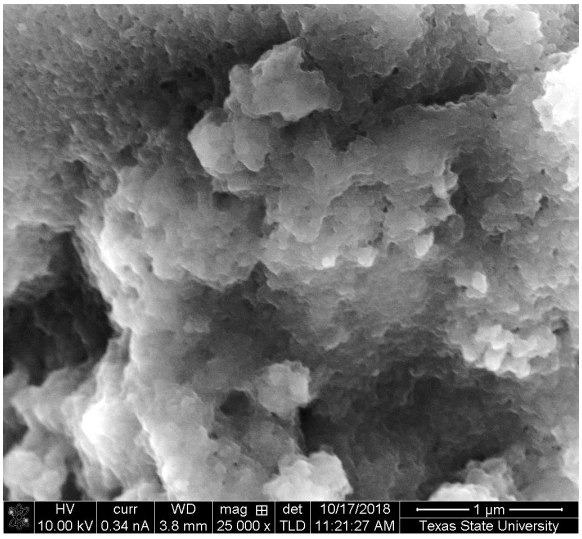

Figure 18**.** SEM image of cassava root treated with 33 % H_3PO_3 at 100 °C for 24h.

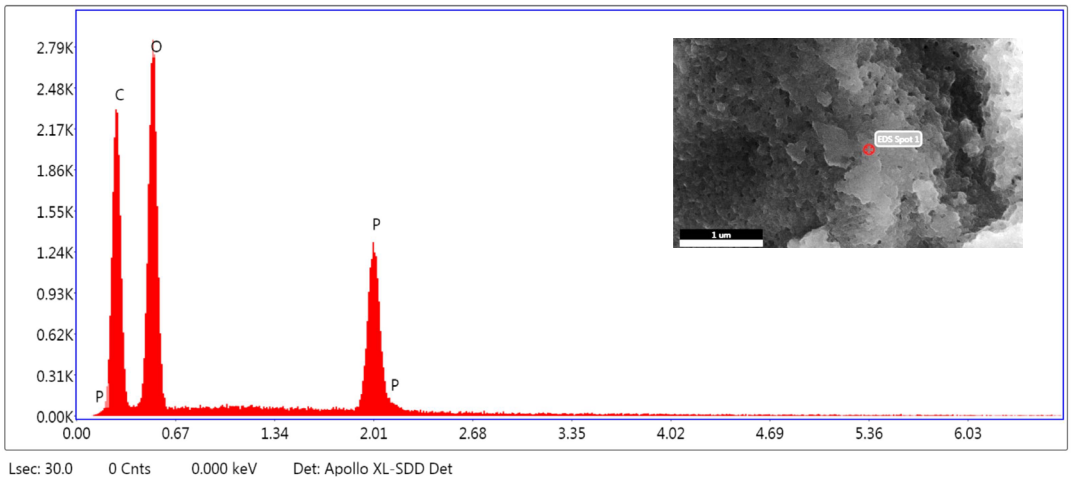

Figure 19**.** EDX spectrum and elemental composition of cassava root treated 33 % H_3PO_3 at 100 °C for 24 h.

After heating TGA data, 5 g of the intermediate material (acid treated cassava root) was exposed to microwave irradiation at 1000 W with 2.45 GHz magnetron for 10 minutes in air. The sample exfoliated and expanded more than 500 vol. % to form sheet-like structure, depicted in Figure 20. A similar results was observed when the acid treated cassava sample was exposed to microwave heating under 50 vol. % H_2 in balance

of Ar. The final solid product after microwave heating was washed thoroughly in 10 vol. % HCl to remove any unreacted precursors and followed by drying in an oven at 100 ^{o}C overnight.

During the microwave irradiation, a substantial amount of H_2O molecules were removed from the pretreated cassava root. Elemental analysis confirmed drastic reduction in oxygen content as showed in Table 2. It appears the acid catalyzed the removal of oxygen-containing groups during microwave irradiation. When the sample was acid treated and was placed on a hot plate at 500 °C in air, minimal expansion of the material with evolution of a substantial amount of gases was observed. SEM image and elemental analysis data revealed heating on hot plate in air resulted in substantial decrease in the carbon content. However, the concentration of oxygen and phosphorus combined were more than 75 at. %. Thus, heating on a hot plate in air resulted in decomposition of carbon to form gases and the remaining carbon formed a dense structure with minimum exfoliation of sheets as shown in Table 2.

Microwave assisted exfoliated cassava extract samples were washed with 10 vol. % HCl to remove excess phosphorous compounds and subsequently rinsed with de-ionized water several times until the pH was about 7. The resulting material retained its sheet-like morphology and carbon composition reached up to 89.3 wt. % as showed in Figure 21 and Table 2. The sample was heat-treated in 50/50 vol. % H_2/Ar at 1000 °C for 1 h to remove any remaining oxygen containing groups. The resulting material was made up of carbon nanosheets containing less than 4 wt. % oxygen as shown by elemental composition data presented in Table 2 and scanning electron micrograph displayed in Figure 22.

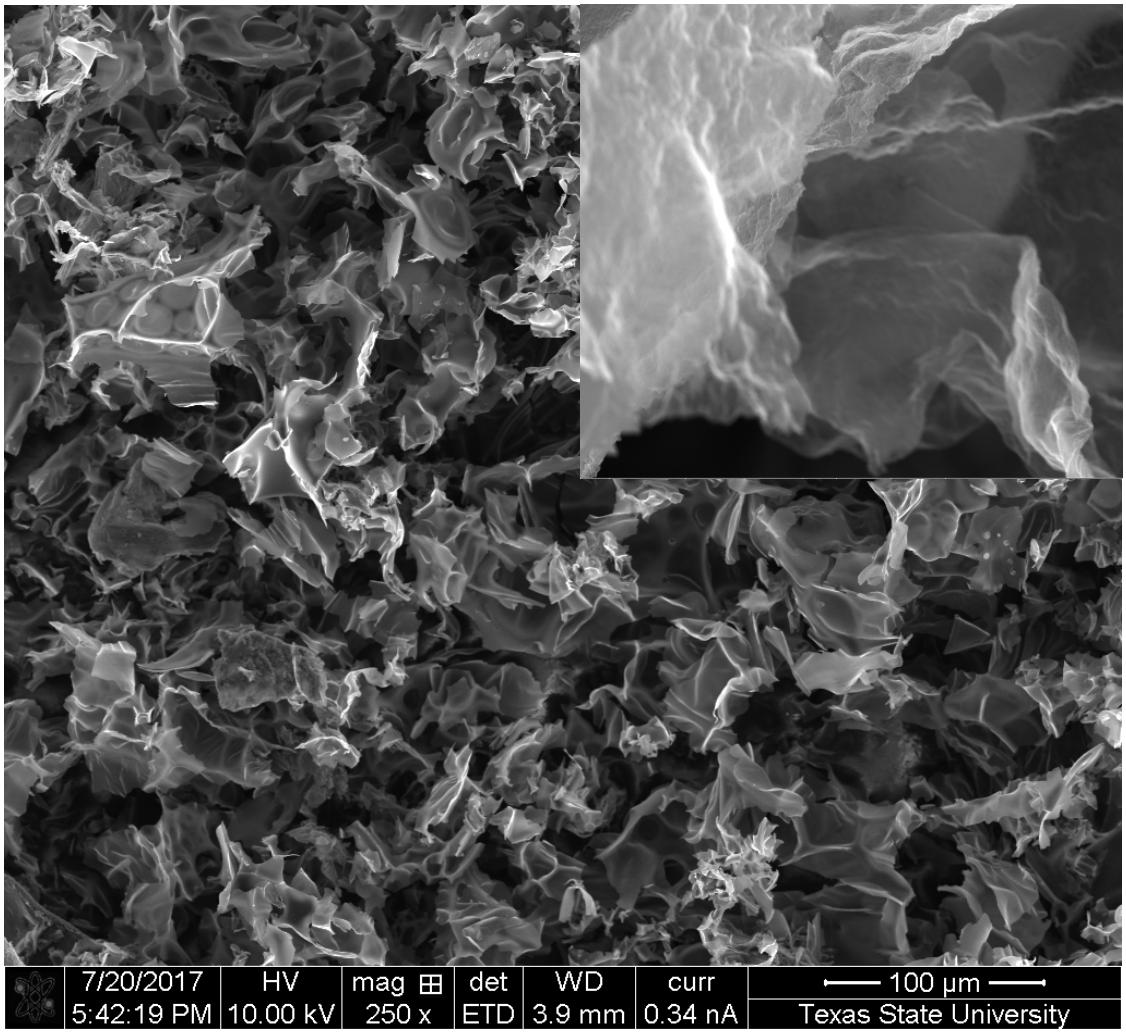

Figure 20**.** SEM image of microwave exfoliated cassava root pretreated with 33 % H_3PO_3 at 100 °C for 24 h.

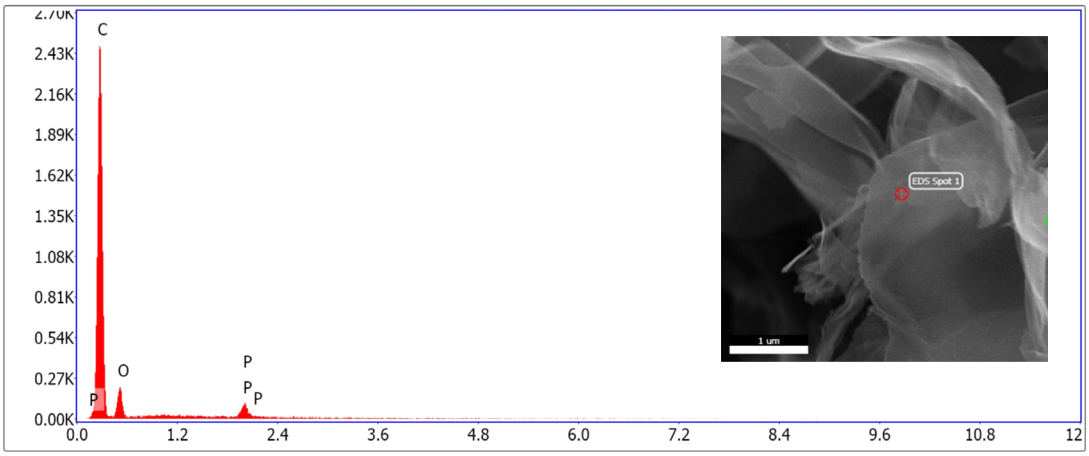

Figure 21. EDX spectrum of microwave exfoliated cassava sample (33.3 % H_3PO_3).

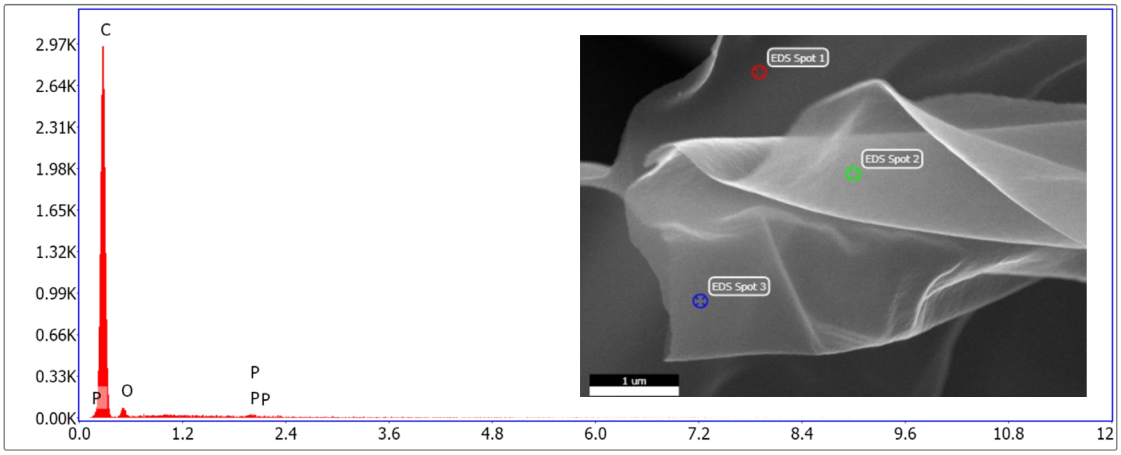

Figure 22. EDX spectrum of microwave exfoliated cassava sample (33.3 % H_3PO_3) exposed to heat treatment at 1000 °C (spot 3).

The microwave-synthesized carbon material prepared from cassava extract were imaged using a transmission electron microscope. The TEM images presented in Figure 23 and 24 clearly show the synthesized materials are made of graphitic carbon nanosheets as evident from the graphitic fringes and interplanar distances.

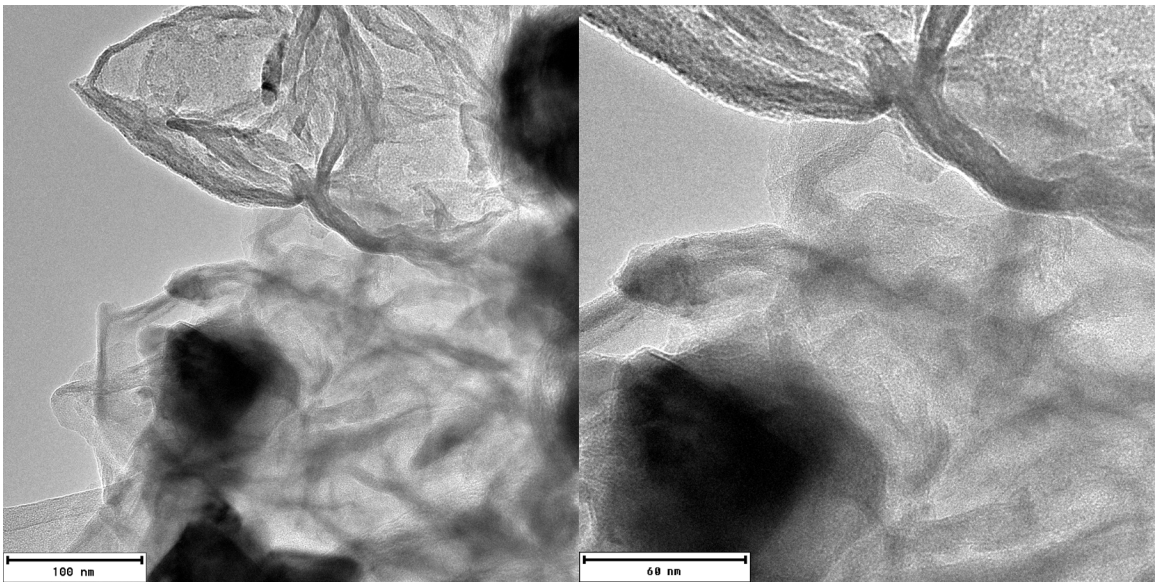

Figure 23. Low resolution TEM images of microwave-exfoliated cassava extract treated with 33.3 % H_3PO_3.

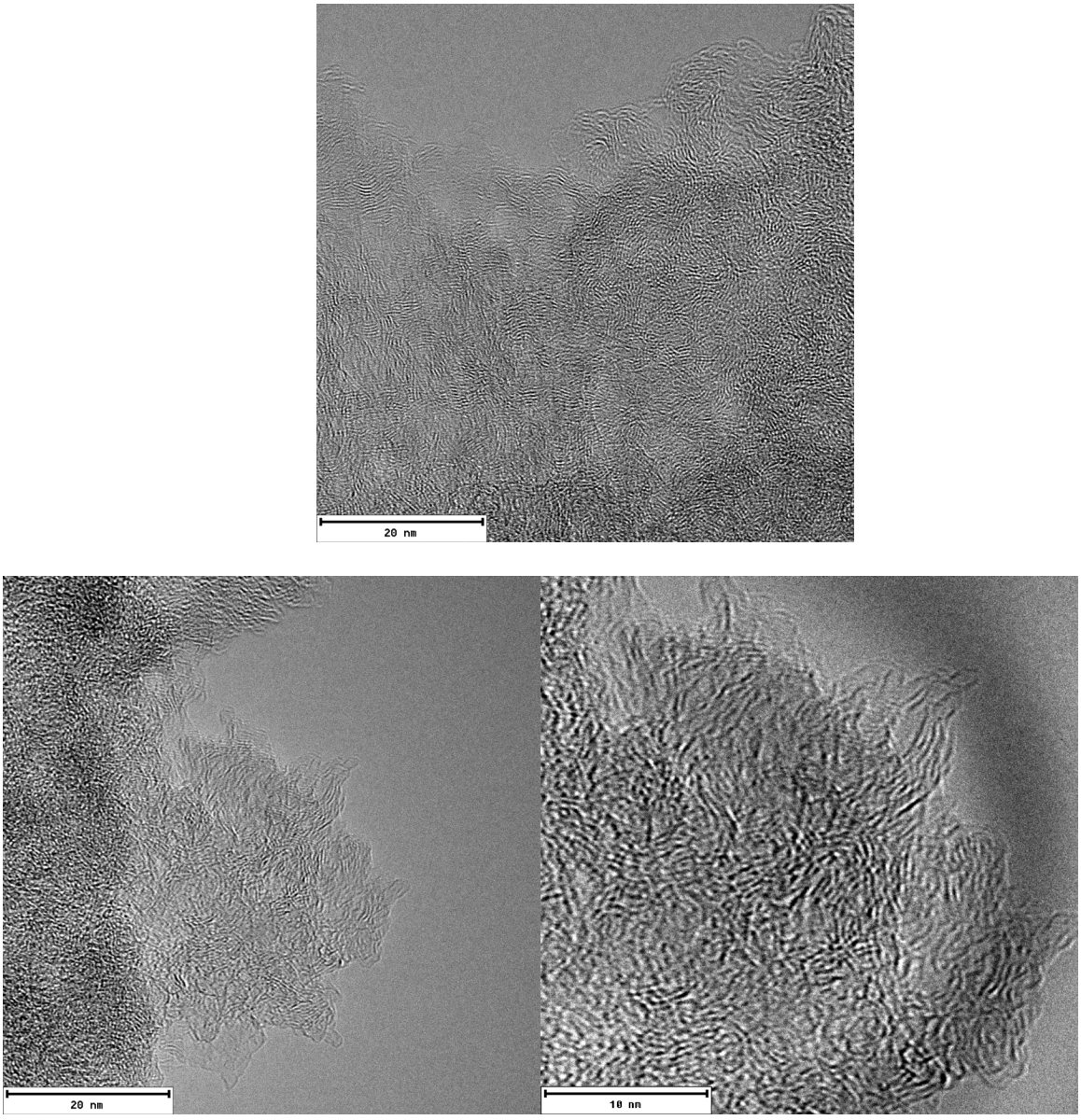

Figure 24. Transmission electron micrograph images of microwave-synthesized carbon nanosheets prepared from of cassava root extract pretreated with 33.3 % H_3PO_3 and exposed to 1000 °C.

Attempts were made to use X-ray diffraction to characterize microwave exfoliated carbon nanosheets obtained by pretreating cassava with 33.3 wt. % H_3PO_3, followed by heat treatment at 1000 °C. The X-ray diffraction pattern (Figure 25) of the resulting material shows two peaks at $2\boldsymbol{\theta}$ of 25.06 °, and 43.8 ° that correspond to crystallographic planes (002) and (101) of graphitic material, respectively. Plane (002) has *d*-spacing of 3.5496 Å and (101) has *d*-spacing of 2.0652 Å. The crystallite size is typically estimated from the X-ray diffraction peak by using the Scherrer equation. The Scherrer equation was published in 1918 [81] and states that peak width (*B*) is inversely proportional to crystallite size (*L*).

$$B(2\theta) = \frac{K\lambda}{L\cos\theta}$$

When both crystallite size broadening and microstrain broadening are present, a Williamson-Hall Plot is used. In the absence of strain, the Williamson-Hall Plot reduces to the Scherrer Equation. The crystallite size was estimated to be 0.391 nm and the strain was zero in the sample.

$$B = \left[\frac{K\lambda}{L\cos\theta} + \left(4\varepsilon\frac{\sin\theta}{\cos\theta}\right)\right]$$

No.	2-theta(º)	d(ang.)	Height(counts)	FWHM(º)	Size (ang.)	Phase name
1	25.0667	3.54963	9.902948	1.13973	74.5783	Graphite(0,0,2)
2	43.8	2.06521	14.845120	1.13973	78.4633	Graphite(1,0,1)

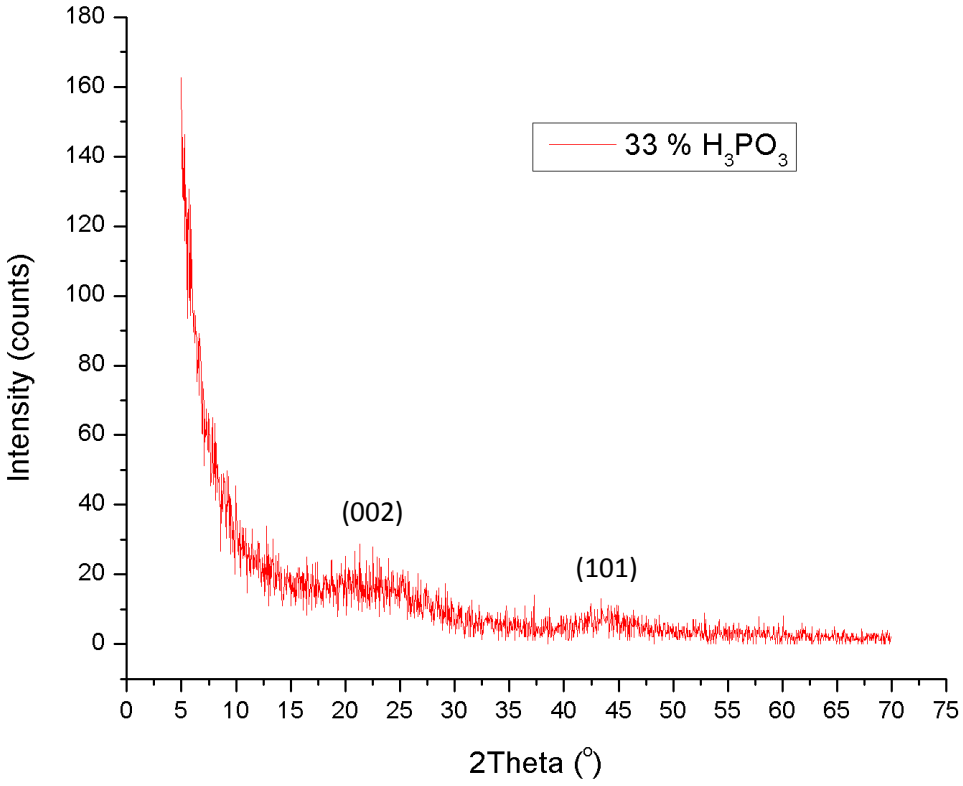

Figure 25. X-ray diffraction pattern of cassava extract pretreated with 33 wt. % H_3PO_3, microwave exfoliated, and subsequently heat treated at 1000 °C.

Raman spectroscopy was used to probe the chemical bonds in synthesized carbon nanosheets. Figure 26 shows Raman spectra of carbon nanosheets obtained after microwave heating of cassava extract pretreated with 33.3 % H_3PO_3. It can be seen clearly that from Figures 26-27, the characteristic peak at ~1343 cm^{-1} and ~1598 cm^{-1} representing D-band and G-band in carbon are present in all the samples. The G-band is present in sp^2 bonded carbons, whereas the D-band originated from hybridized vibrational mode related to the graphene edges and thus reveals the presence of disorder in the graphene structure [47-49].

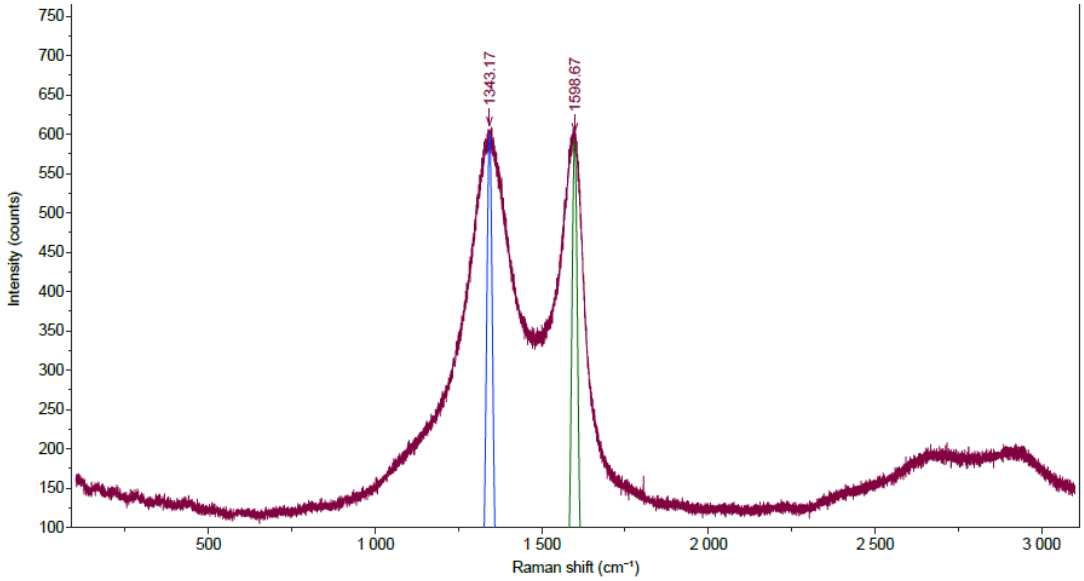

Figure 26. Raman spectra of carbon nanosheets obtained by microwave exfoliation of cassava extract pretreated with 33 wt. % H_3PO_3.

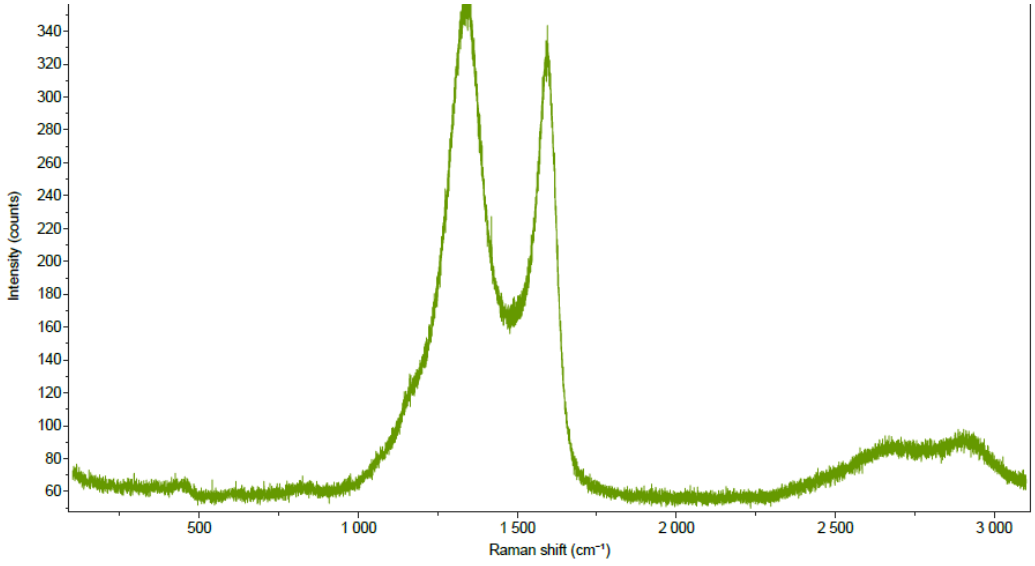

Figure 27. Raman spectra of carbon nanosheets obtained by microwave exfoliation of cassava extract pretreated with 33 wt. % H_3PO_3, and subsequently exposed to heat treatment at 1000 °C.

Table 3. Raman data of carbon nanosheets obtained by microwave exfoliation of cassava extract and subsequently exposed to heat treatment at different temperatures.

Wt. % H_3PO_3	Processing Conditions	D-Band (cm^{-1})	G-Band (cm^{-1})	Intensity I_D/I_G
33.3	Microwave synthesis	1356	1596	0.96
33.3	Heat treated at 900 °C after microwave synthesis	1343	1591	1.02
33.3	Heat treated at 1000 °C after microwave synthesis	1343	1591	1.08

In addition, it was observed that the crystallinity and graphitization of the carbon nanosheets increased with increasing heat treatment temperature after heating the microwave synthesis. It can be seen clearly that the D-band and G-band of carbon nanosheets heated after microwave synthesis exhibited narrow width at half-maximum (FWHM) values compared with the microwave synthesized sample without heat treatment. In addition, the D-band increased in intensity drastically. This increase in D-band intensity is due to removal of remaining oxygen-containing groups in the carbon sample and termination of the edges of the carbon nanosheets. This is consistent with Raman observation of graphene edges, showing a large D-band intensity [6, 47-49]. In addition, the ratio of the intensity of the D-band to G-band increased with increasing heat treatment temperature as seen in Table 3. It should be noted that the ratio of D-band to G-band can be a good indicator of the level of ordering/graphitization in carbon materials typically seen in the graphite powder sample [47-49]. However, it has been observed that

a nonporous microcrystalline natural graphite sample also shows a much larger D-band intensity when compared to its G-band [82-85], due to the small crystal grains in the structure. Estevez *et al.*, argued that natural graphite is made up of small graphitic domains that lead to a misdiagnosis of the material being non graphitic if one only analyzes the ratio of the D- and G-bands [82]. Estevez *et al.* indicated that a highly porous graphitic carbon can be thought to be comprised of "small crystalline domains", with the well-ordered/graphitic carbon located in between the small nanometer pores and concluded that the narrowness of the G and D peaks, and the presence of a G′ band (~2700 cm^{-1}) is a good indicator of the graphitic ordering for the porous carbons [82].

In the FT-IR spectra presented in Figure 28. It can be seen clearly that cassava extract treated with H_3PO_3 showed a broad peak at 2335 cm^{-1} due to stretching vibrations of P−OH and P-H functionalities [70]. The broad band observed between 2923 and 2852 cm^{-1}, is attributed to the CH_2 stretching vibration and CH stretching vibrations. Also, carboxylic acids and carbonyl groups (-C=O) are seen at 1712 cm^{-1}. The –OH stretching of carboxylic acid typically seen at 3340 cm^{-1} is observed as a broad peak because of other OH contributions in the acid treated material.

The presence of a band at 1591 cm^{-1} corresponds to the C-C non-oxidized graphitic domain in the sample. In addition, 1037 cm^{-1} is attributed to stretching vibration of C-O. In addition, -OH bending appears at 1637 cm^{-1} and residual -OH from P-OH and C-OH shows at 1127 cm^{-1}. The band at 995 cm^{-1} represents P=O and epoxy groups while 886 cm^{-1} indicates the presence of P-OH vibrations.

It can be seen that after thermal treated at 1000 °C, all the peaks disappeared except 1037 cm^{-1} due to removal of oxygen-containing functional groups. The

appearance of C-O stretching vibration at 1037 cm^{-1} after thermal treatment is due to oxygen attached to the edges of the nanosheets.

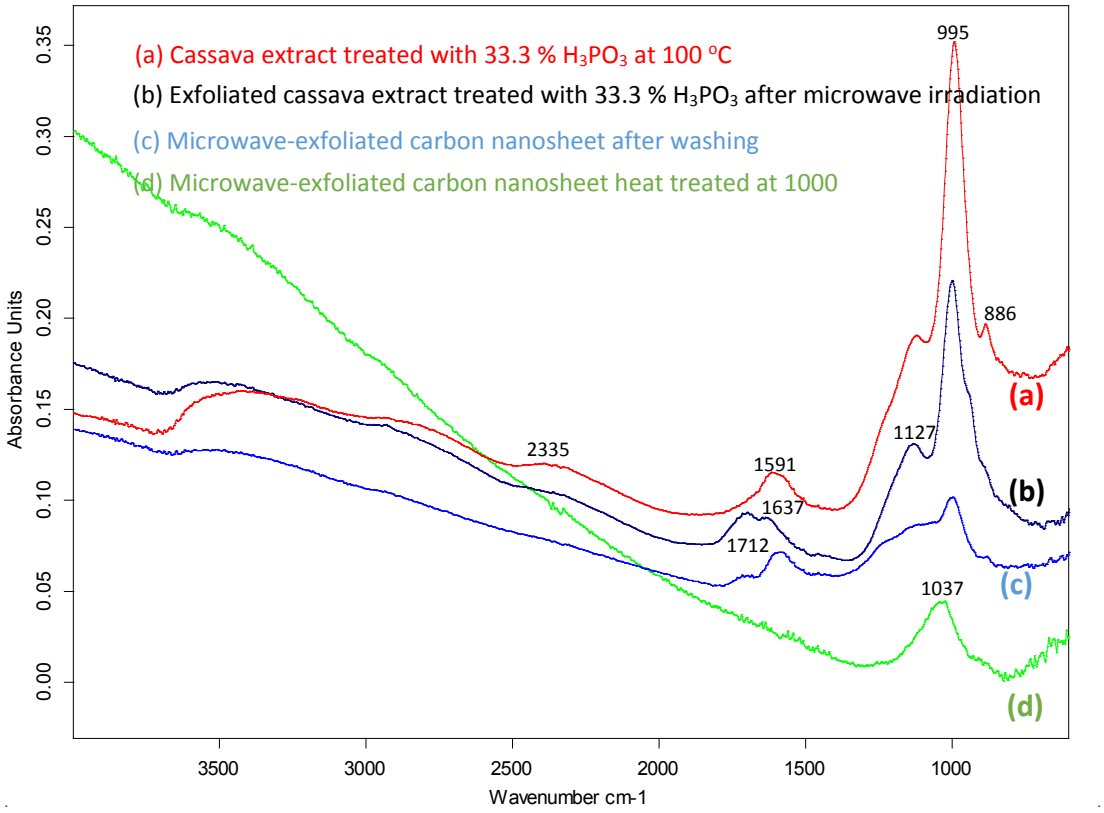

Figure 28 FT-IR spectra obtained from cassava extract at different stages during synthesis of carbon nanosheets.

The nitrogen gas adsorption data of various carbon-based products are presented in Tables 4 and 5. The data shows that high surface area carbon nanosheet can be synthesized from cassava extract via a thermochemical activation process. When raw cassava extract was directly exposed to 1000 °C in hydrogen atmosphere, the resulting material had a BET surface area of 174 m^2/g. Furthermore, it was observed that microwave synthesis of cassava pretreated with 33.3 wt. % H_3PO_3 resulted in increased

BET surface area to about 237 m^2/g and pore volume to 0.22 cm^3/g. Heat treatment of the microwave-synthesized carbon nanosheet further increased the surface area and pore volume. The gas adsorption data presented in Table 6 and Figure 29 revealed BET surface area of 1941 m^2/g and pore volume of 0.87 cm^3/g for carbon nanosheet sample thermally treated at 1000 ^oC. In addition, BET surface area and pore volume data carbon nanosheet exposed to different temperatures is presented in Table 4. Table 5 also summaries variation of H_3PO_3 content with surface area and pore volume.

It has been reported and demonstrated that high surface areas and large pore volume values are both important in energy storage application [82, 85]. Unfortunately, having both high surface area and large pore volume in one material requires a well-controlled morphology and is very difficult to achieve. Typically high surface areas (> 1500 m^2/g) are usually associated with smaller pores, whereas pore volumes greater than 3 cm^3/g require larger sized pores > 10 nm [82]. The next section explores further engineering of carbon nanosheets with both high surface area (> 2000 m^2/g) and large pore volume (> 3 cm^3 /g) for potential applications in energy storage devices.

Table 4. Summary of nitrogen gas adsorption isotherm data of carbon nanosheets prepared with different content of H_3PO_3.

Wt. % H_3PO_3	Processing Conditions	BET Surface Area m^2/g	Pore Volume cm^3/g
33.3	Heat treated 800 °C after microwave synthesis	233.8	0.214
33.3	Heat treated 900 °C after microwave synthesis	365.1	0.270
33.3	Heat treated 1000 °C after microwave synthesis	1941.5	0.870

* refers to wt. % H_3PO_3 in balance of cassava extract, on water free basis

Table 5. Summary of nitrogen gas adsorption isotherm data of carbon nanosheets heat treated at different temperatures.

Wt. % H_3PO_3	Processing Conditions	BET Surface Area m^2/g	Pore Volume cm^3/g
0.00	Pyrolyzed at 1000 °C	174.0	0.087
33.3	Exposed to microwave heating	237.2	0.218
33.3	Exposed to 1000 °C after microwave synthesis	1941.5	0.870
42.9	Exposed to 1000 °C after microwave synthesis	637.3	0.470
50.0	Heat treated 1000 °C after microwave synthesis	242.1	0.265

* refers to wt. % H_3PO_3 in balance of cassava extract, on water free basis

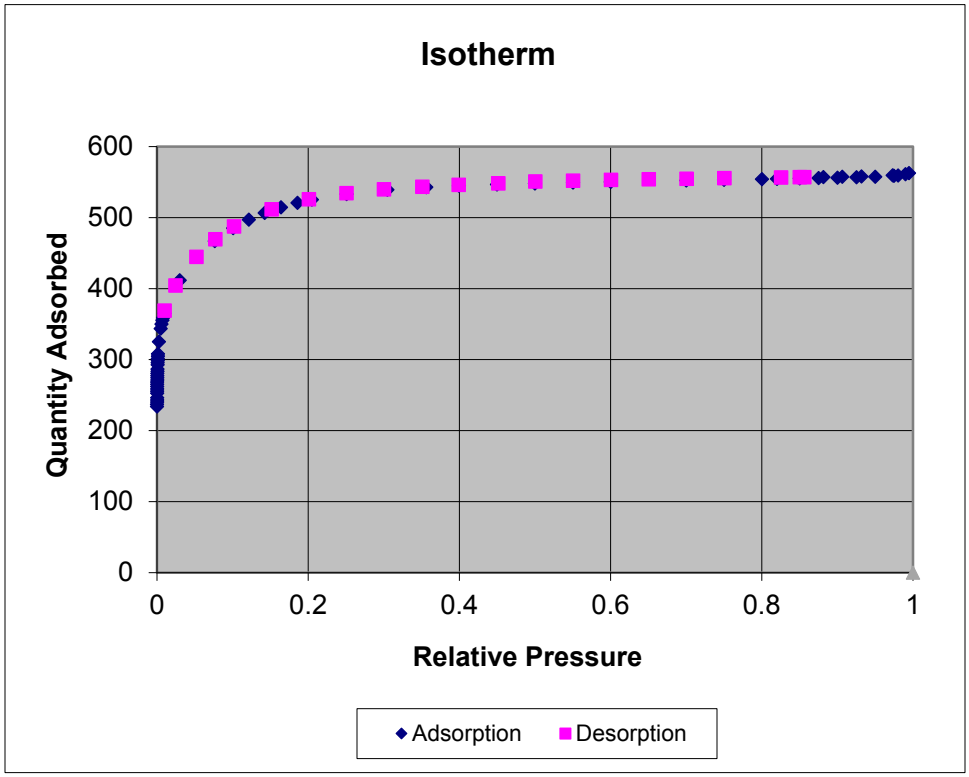

Figure 29. Nitrogen gas adsorption isotherm of microwave-exfoliated cassava sample (33 wt. % H_3PO_3) exposed to heat treatment at 1000 ºC.

Table 6**.** BET specific surface area data of carbon nanosheet obtained from microwave-exfoliated cassava (33 wt. % H_3PO_3) exposed to heat treatment at 1000 ºC.

BET Surface Area (m^2/g)	**1941.5 ± 11.6**
C	**343.6**
Qm (cm^3/g STP)	**446.0**
Slope (g/cm^3 STP)	0.002235625
Y-Intercept (g/cm^3 STP)	0.000006525
Correlation	0.999939052
Molecular CSA (nm^2)	0.162

4.3 Characterization Cassava Extract and H_3PO_4

In this research, a total of 60 g of cassava extract was added to 200 mL of phosphoric acid and stirred thoroughly. The mixture was exposed to 160 ^oC for 3 h in a convection oven in air atmosphere to form an intermediate mixture. The bulk sample of intermediate material was heat treated based on the TGA data presented in Figure 13.

A sample size of 40 g of intermediate mixture was put in a quartz combustion boat and placed inside quartz tube for heat treatment. The intermediate sample was ramped at 15 ^oC/min from 20 ^oC to 1000 ^oC and held at 1000 ^oC for 1 h. The thermal treatment was carried out in a gas mixture containing 50 vol. % argon and 50 vol. % hydrogen gas, flowing at a total rate of 1000 L/min. The final solid product after heating was washed thoroughly in 10 vol. % HCl and rinsed with deionized water. This was followed by a second heat treatment in inert atmosphere at 1000 ^oC for 3 h. X-ray diffraction pattern of the resulting carbon nanosheet is displayed in Figure 30 shows extremely low diffraction peak intensities of (002) and (101) planes, confirming the sample is made up of a few layers of carbon nanosheets. In addition, X-ray photoelectron spectrum data presented in Figures 31-33 confirmed the resulting product has more than 97.9 % carbon content, which is composed of mainly carbon-carbon bonding.

Figure 34 presents evidence of graphitic layers in high resolution transmission electron micrograph of the carbon nanosheets prepared from cassava extract treated with 81 % H_3PO_4 and pyrolyzed at 1000 ^oC.

In addition, the intermediate materials were pyrolyzed at different temperatures. Figure 35-37 show SEM images of intermediate material pyrolyzed at 550 ^oC, 850 ^oC, and 1000 ^oC, respectively. It was observed that the morphology of the carbon

nanomaterial is formed by 550 ^{o}C, which is consistent with the TGA data. Further heating of the sample decomposes and removes the remaining H_3PO_4, P_2O_5, and oxygen-containing groups in the samples. This was evident in the elemental composition analysis of the sample presented in Table 7.

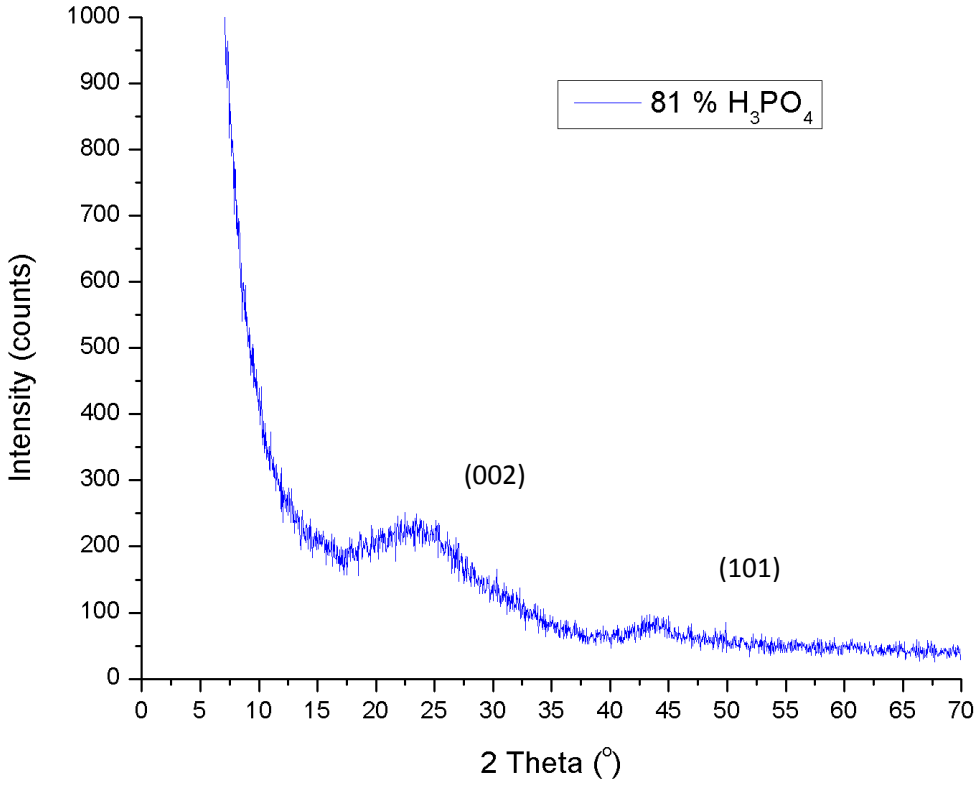

Figure 30. X-ray diffraction pattern of carbon nanosheet prepared from cassava extract treated with 81 % H_3PO_4 and pyrolyzed at 1000 ^{o}C.

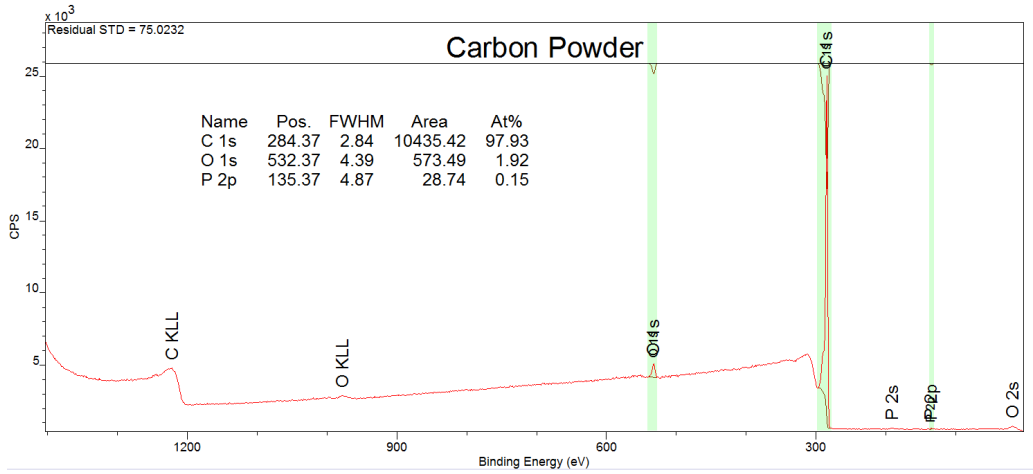

Figure 31. X-ray photoelectron survey spectrum of carbon nanosheet produced from cassava extract treated with 81 % H_3PO_4 and pyrolyzed at 1000 ^oC.

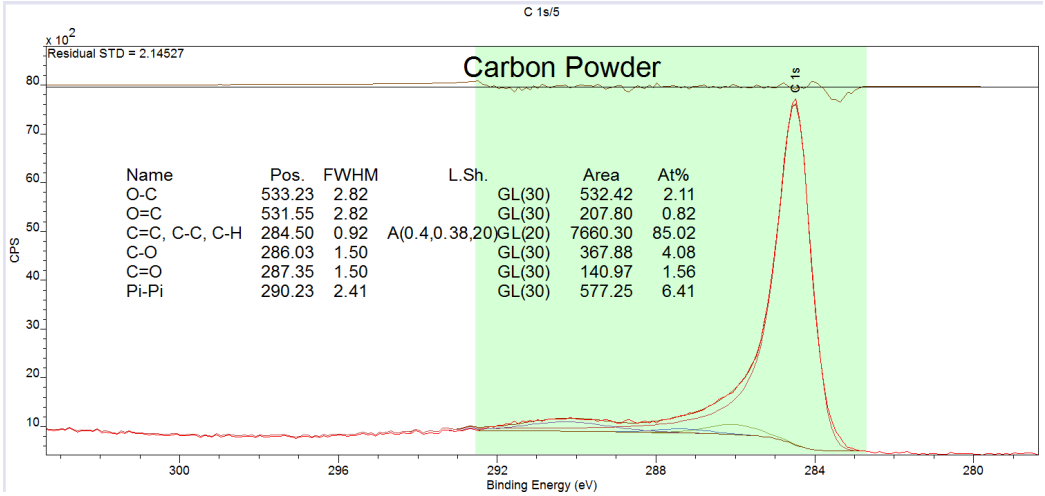

Figure 32. High-resolution X-ray photoelectron carbon spectrum of carbon nanosheet produced from cassava extract treated with 81 % H_3PO_4 and pyrolyzed at 1000 ^oC.

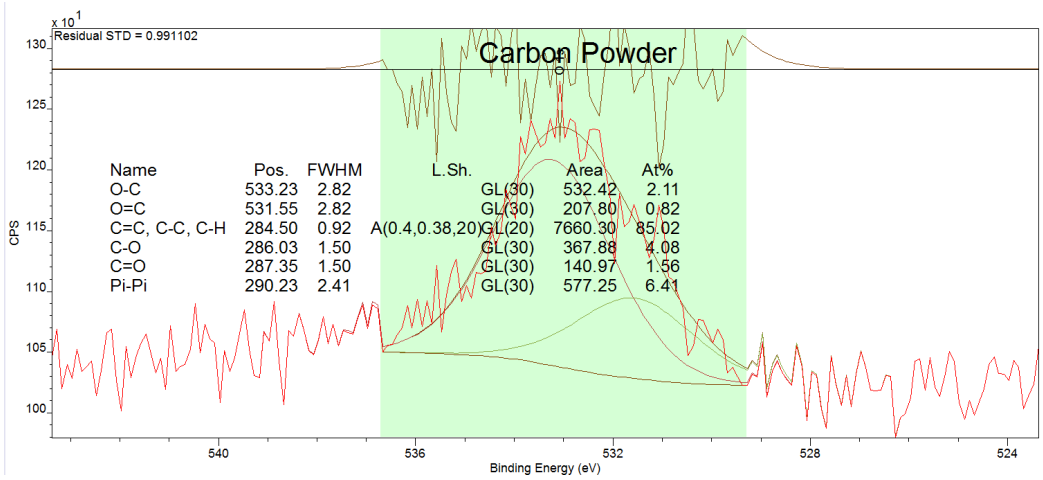

Figure 33. High-resolution X-ray photoelectron oxygen spectrum of carbon nanosheet produced from cassava extract treated with 81 % H_3PO_4 and pyrolyzed at 1000 ^oC.

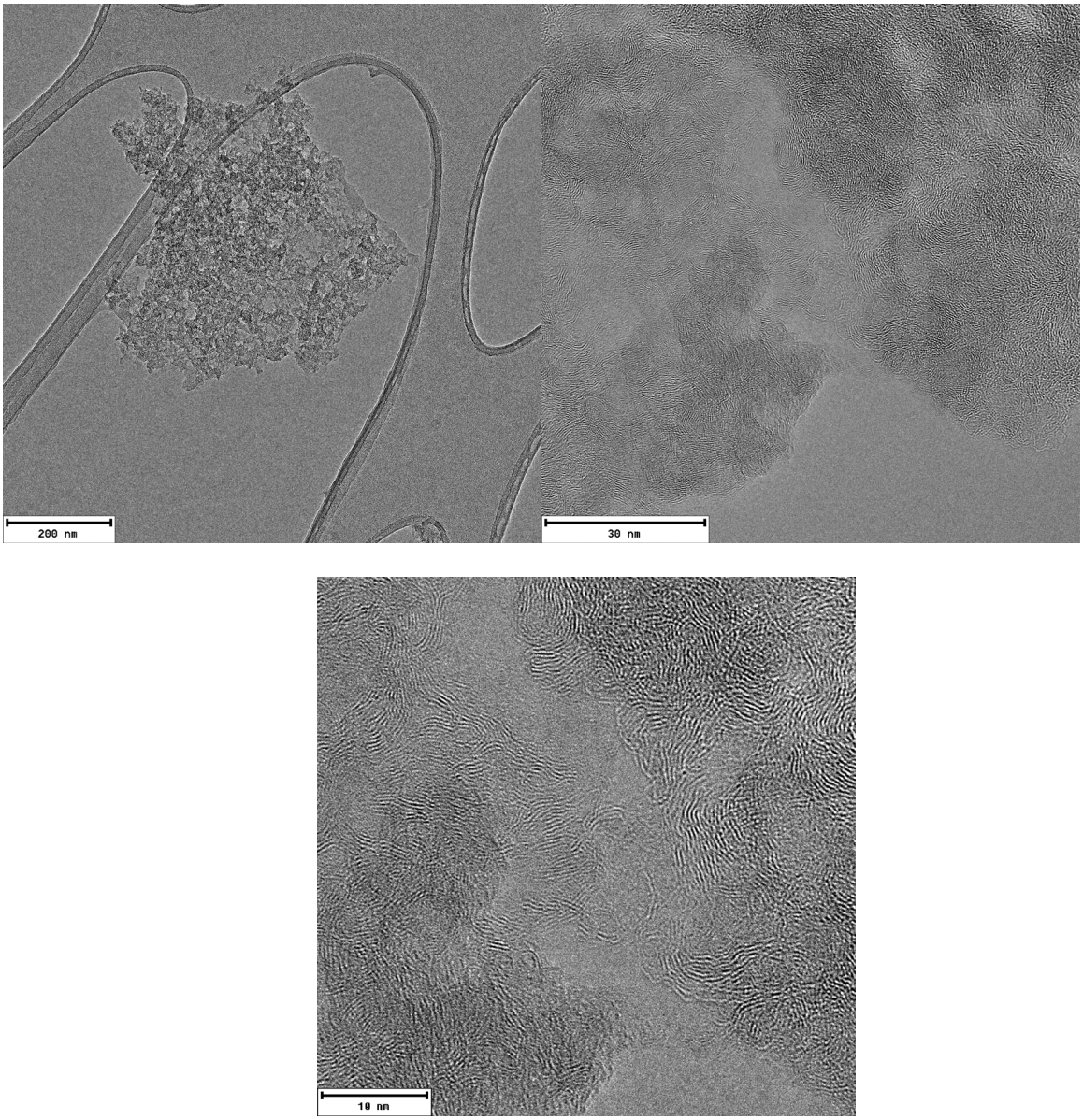

Figure 34. High resolution transmission electron micrograph showing graphitic sheets of carbon produced from cassava extract treated with 81 % H_3PO_4 and pyrolyzed at 1000 ^oC.

.

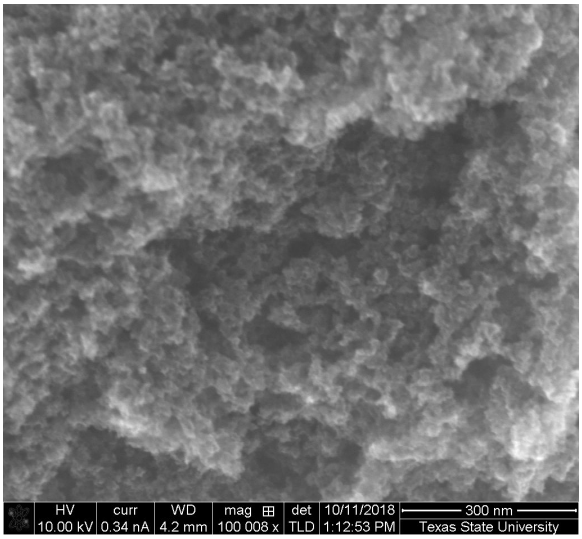

Figure 35. Scanning electron micrograph showing graphitic sheets of carbon produced from cassava extract treated with 81 % H_3PO_4 and pyrolyzed at 550 °C.

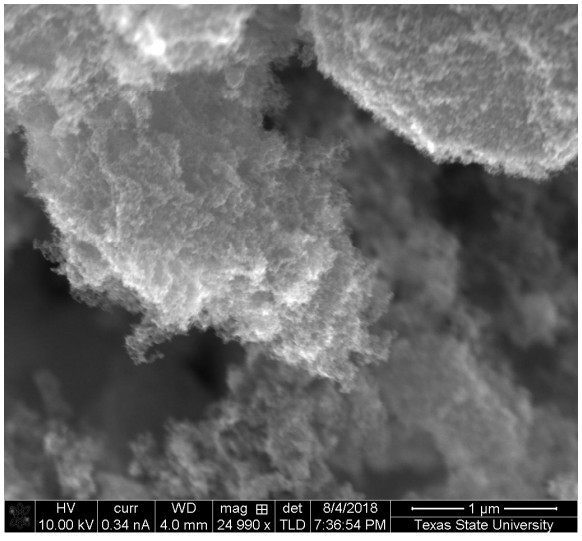

Figure 36. Scanning electron micrograph showing graphitic sheets of carbon produced from cassava extract treated with 81 % H_3PO_4 and pyrolyzed at 850 °C.

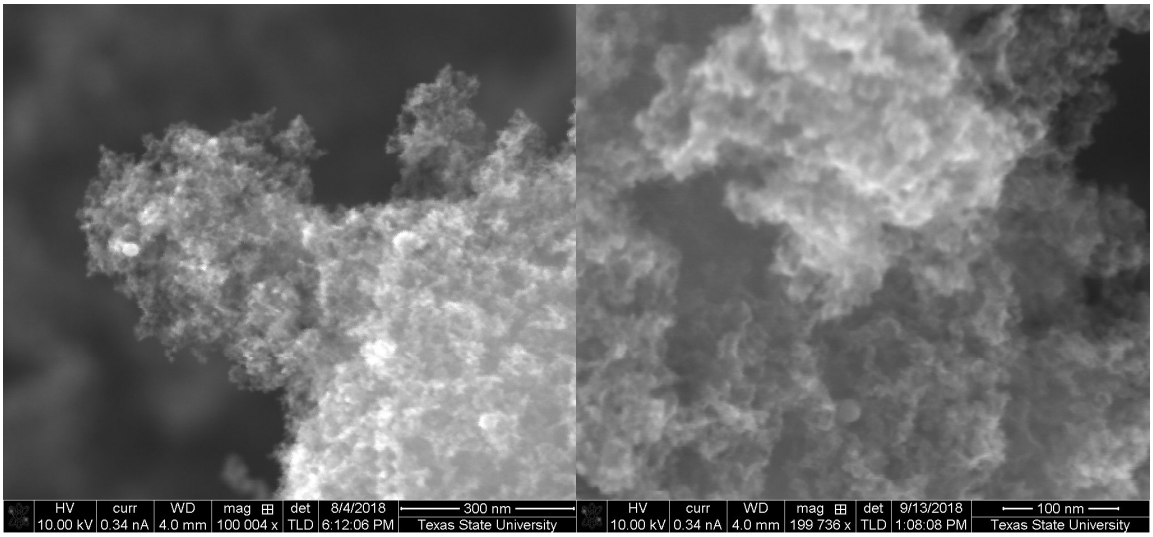

Figure 37. Scanning electron micrograph showing graphitic sheets of carbon produced from cassava extract treated with 81 % H_3PO_4 and pyrolyzed at 1000 °C.

Table 7. Elemental composition of carbon nanosheets prepared at different temperatures.

Wt. % H_3PO_4	Temperature (°C)	C (at. %)	O (at. %)	P (at. %)	Si (at. %)
81.1	550	84.51	12.65	2.85	-
81.1	850	92.20	6.74	0.16	0.91
81.1	1000	94.07	5.93	-	-

The BET surface area and pore volume of the resulting samples also increased with increasing pyrolysis temperature as presented in Table 8. It appears removal of oxygen-containing groups creates more pathways as the gases escape and thereby increase the number of available sites of the carbon nanosheets. The nitrogen gas adsorption data showed specific surface areas of up to 2956 m^2/g and pore volumes of 5.1 mL/g in carbon nanosheets after thermal treatment at 1000 °C. The Raman data also clearly shows that increasing the pyrolysis temperature leads to more defects in the resulting nanosheets. Specifically, the D-band of the nanosheet increased in intensity with respect to the G-band when the temperature was increased from 550 °C to 1000 °C. Summary of the Raman data is presented in Figure 38 and Table 9.

Table 8. BET surface area and pore volume data of carbon nanosheets synthesized at different temperatures.

Wt. % H_3PO_4	Processing Conditions	BET Surface Area m^2/g	Pore Volume cm^3/g
81.1	Directly pyrolyzed at 550 °C	700.4	1.887
81.1	Directly pyrolyzed at 850 °C	1259.8	2.634
81.1	Directly pyrolyzed at 900 °C	1426.4	2.637
81.1	Directly pyrolyzed at 1000 °C	2956.1	5.112

* refers to wt. % H_3PO_4 in balance of cassava extract, on water free basis

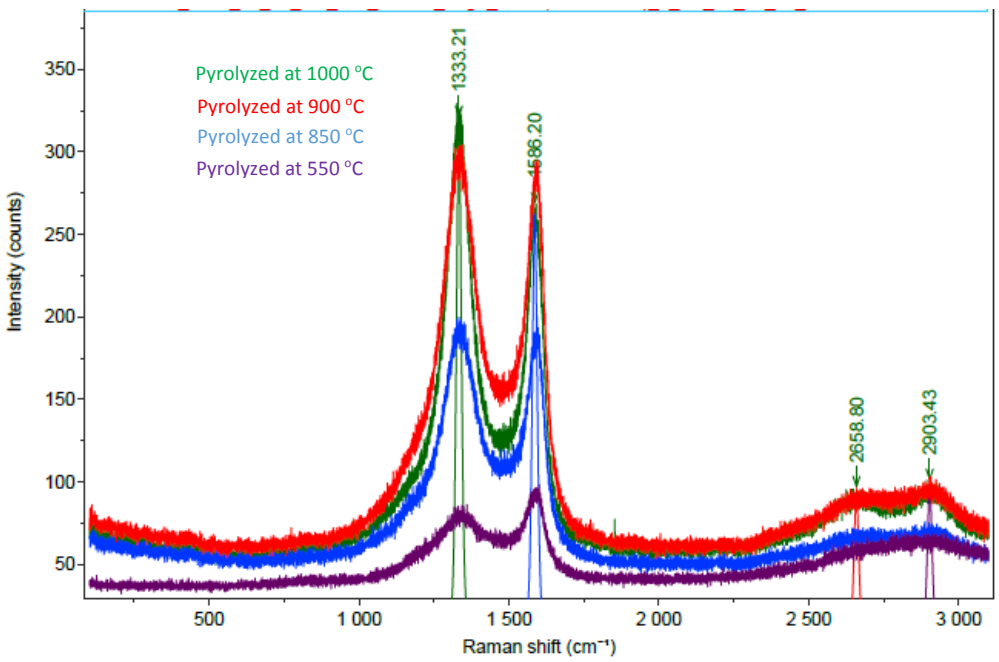

Figure 38. Raman spectra of carbon nanosheets synthesized at different temperatures.

Table 9. Raman data of carbon nanosheets synthesized at different temperatures.

Wt. % H_3PO_4	Processing Conditions	D-Band (cm^{-1})	D-Band Intensity	G-Band (cm^{-1})	G-Band Intensity	I_D/I_G
81.1	Directly pyrolyzed at 550 °C	1334	47.4	1590	59.06	0.80
81.1	Directly pyrolyzed at 850 °C	1333	148.17	1592	144.69	1.02
81.1	Directly pyrolyzed at 900 °C	1335	243.17	1590	230.54	1.05
81.1	Directly pyrolyzed at 1000 °C	1333	269.45	1588	209.16	1.29

During optimization of the concentration of H_3PO_4 in the starting cassava extract slurry, all process conditions were maintained and only the amounts of the H_3PO_4 in the slurry were varied. The nitrogen gas adsorption isotherms of the resulting carbon nanomaterials were measured and the surface areas and pore volumes were evaluated. Table 10 shows the BET surface area and pore volume data. The data indicated that increasing the content of H_3PO_4 from 0 to 45 % increases linearly the surface area and pore volume. Further increase in H_3PO_4 from 45 % to 66 % decreased the BET surface area from 2080 m^2/g to 1547 m^2/g. However, the pore volume was increased by 2 fold to 2.4 mL/g. The highest surface area and pore volume were measured in samples prepared from cassava extract treated with 81 % H_3PO_4. Figure 39 shows the adsorption isotherm of carbon nanosheet obtained by processing cassava extract slurry containing 81 % H_3PO_4 and pyrolyzed at 1000 °C. The evaluated surface area of this sample was 2956 m^2/g and pore volume was 5.1 mL/g.

Table 10. Summary of nitrogen gas adsorption isotherm of carbon nanosheet synthesized by treating cassava extract with different amounts of H_3PO_4.

Wt. % H_3PO_4	Processing Conditions	BET Surface Area (m^2/g)	Pore Volume (cm^3/g)
0.0	Pyrolyzed at 1000 °C	174.0	0.087
10.7	Pyrolyzed at 1000 °C	461.2	0.182
19.3	Pyrolyzed at 1000 °C	818.5	0.343
32.3	Pyrolyzed at 1000 °C	1620.0	0.845
45.5	Pyrolyzed at 1000 °C	2080.3	1.213
66.5	Pyrolyzed at 1000 °C	1547.2	2.426
70.5	Pyrolyzed at 1000 °C	1703.6	2.408
81.1	Pyrolyzed at 1000 °C	2956.1	5.112

* refers to wt. % H_3PO_4 in balance of cassava extract, on water free basis

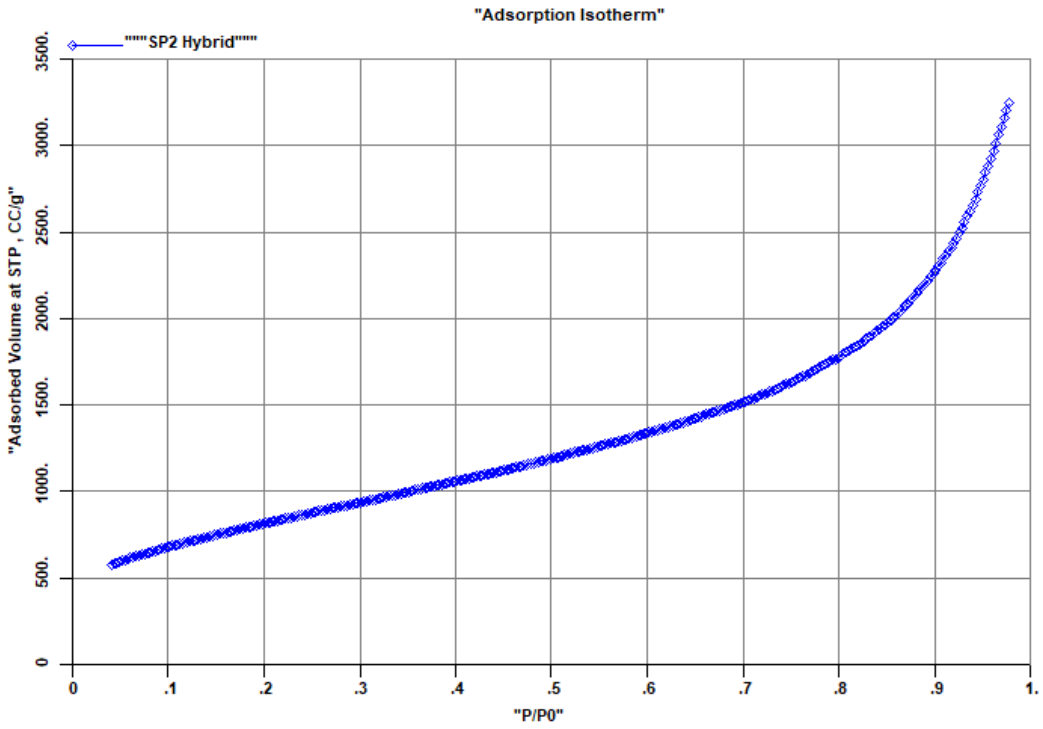

Figure 39. A nitrogen gas adsorption isotherm of carbon nanosheet with BET surface area of 2956 m^2/g and pore volume of 5.1 mL/g.

Figure 40 shows FT-IR spectra of raw cassava extract and carbon nanosheet obtained from acid (H_3PO_4) treated cassava extract pyrolyzed at 1000 ^oC. The IR peak of the raw cassava extract shows a typical polysaccharide. The peaks at 852 cm^{-1}, 928 cm^{-1} and 994 cm^{-1} are attributed to C-O of epoxy and peroxide stretching or scissoring deformation of CH_2. The band at 1079 cm^{-1} and 1149 cm^{-1} represent –C-O-C stretching typically observed in primary and secondary alcohols. In addition, 1243 cm^{-1} and 1637 cm^{-1} are contributions form OH bending in raw cassava extract. Furthermore, -C-CH_3 stretching vibration is seen at 1353 cm^{-1}, while –CH_2 scissor deformation vibration or vibration in benzene moiety appears at 1416 cm^{-1}. The band 2929 cm^{-1} corresponds to saturated C-H stretching due the asymmetric and symmetric CH_2 stretching of glucose

monomer [70]. The IR peak at 1729 cm^{-1} is attributed to (-C=O) of carboxylic acids and carbonyl groups in the cassava extract. In addition, the O-H stretching vibration of carboxyl usually observed at 3301 cm^{-1} is broadened between 3500 cm^{-1} and 2500 cm^{-1}. The absorbance peaks corresponding to O-H stretching (a peak ~3400 cm^{-1}), which is superimposed on the OH stretch of carboxylic acid, is due to the presence of absorbed water molecules and alcohol groups [70].

As expected, only the 1572 cm^{-1} and 1079 cm^{-1} peaks remained after thermal treatment at 1000 °C. The appearance of 1572 cm^{-1} originates from C-C graphitic domain and 1079 cm^{-1} is a contribution from (C-O) due to oxidized edges of the nanosheets.

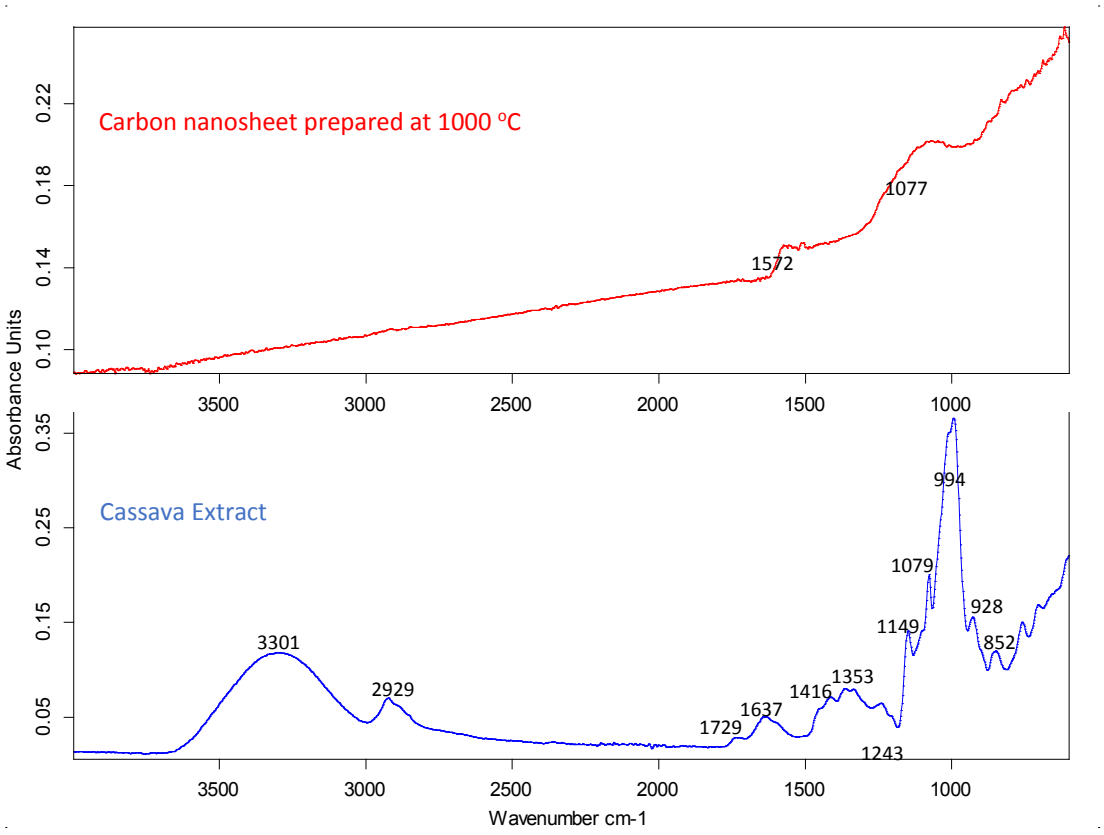

Figure 40. FT-IR spectra of raw cassava extract and carbon nanosheet prepared from acid treated cassava extract pyrolyzed at 1000 °C.

4.4 Catalyst-Free Growth of Wrapped-Graphene Sheets from Renewable Carbon Source

In this research, carbon nanosheets with different morphologies were grown from renewable carbonaceous materials such as cassava extract, rice grain and corn without using any catalyst. About 5 g of cassava extract was heated slowly from room temperature at a rate of 15 °C/min to 1000 °C in a reducing atmosphere comprised of 100 % hydrogen gas flowing at 100 ml/min. The sample was held at 1000 °C for 1 h in reducing atmosphere, then cooled down to room-temperature under inert atmosphere. Figure 41 shows an electron micrograph of the resulting wrapped graphene sheet-like structure mixed with bulk sheets substrate. The SEM image in Figure 40 gives an insight into how these wrapped-graphene sheet are grown from the bulk carbon substrate.

Although the mechanism of grown is not fully understood at this time, a "hurricane growth mechanism" is proposed. It is hypothesized that during heating of the carbonaceous material in reducing atmosphere, the carbonyl groups and other oxygen-containing groups in the samples reacted with hydrogen at elevated temperatures to form water and release at lot of free carbon. The water vapor forces its way out of the carbonaceous substrate leaving pores and vents in the substrate. In the process, the cloud of water vapor forms a nano-hurricane around the pores and vents, and free carbon begins to grow graphene sheets around the vents of the nano-hurricane. Over time, the seed of graphene sheets grow to form wrapped-graphene sheets following the path of gases venting from the pores of the carbon substrate. Figures 43-44 show SEM images of wrapped- graphene sheets formed from pyrolysis of rice grain and corn, respectively, at 1000 °C for 3 h in reducing atmosphere.

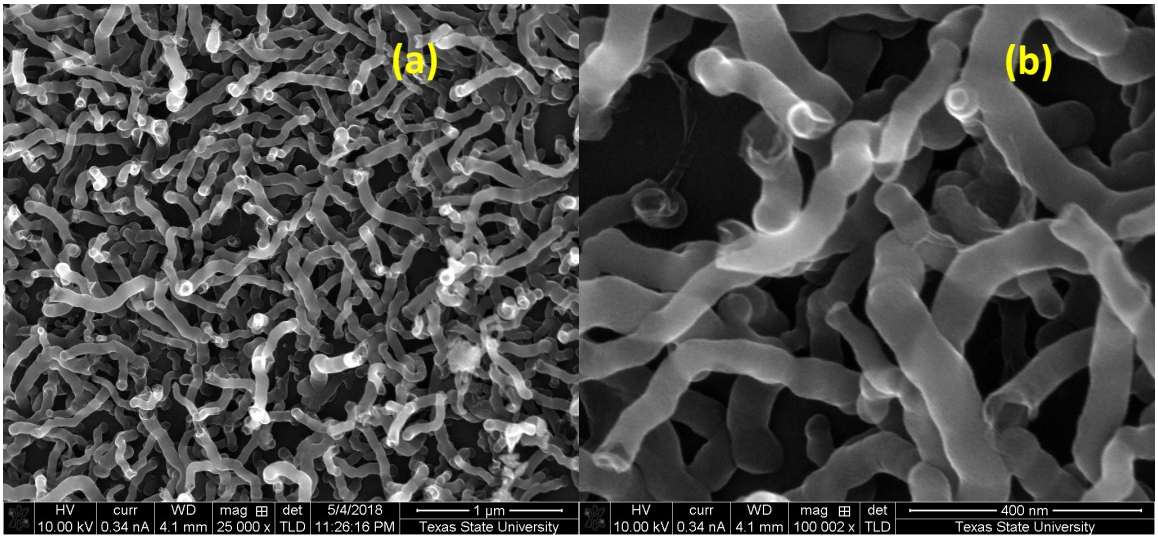

Figure 41. Scanning electron micrograph images showing graphene sheets and wrapped-graphene sheets prepared from cassava extract only at 1000 °C taken at different magnifications, (a)25,000X and (b)100,002X.

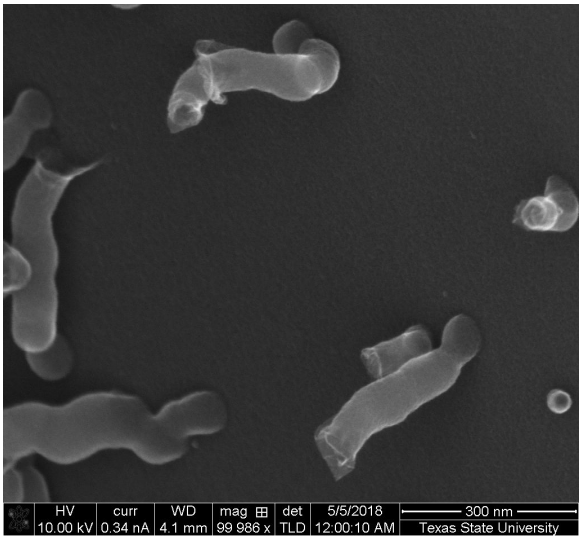

Figure 42. A scanning electron micrograph showing growth of wrapped-graphene sheets prepared from a renewable carbonaceous material at 1000 °C.

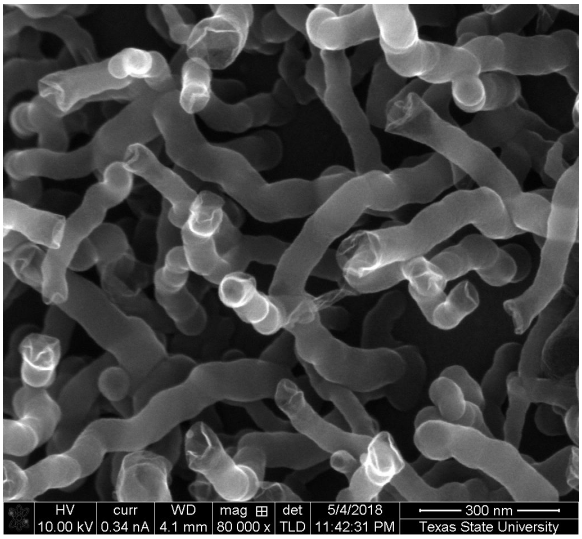

Figure 43. A scanning electron micrograph wrapped-graphene sheets grown from rice grain only at 1000 °C.

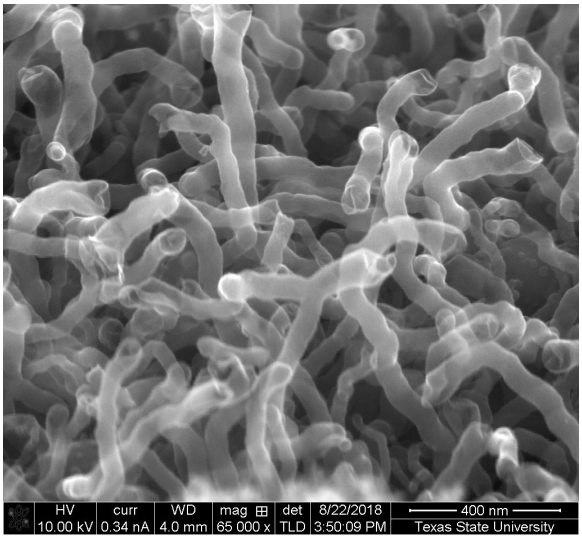

Figure 44. A scanning electron micrograph wrapped-graphene sheets grown from corn grain only at 1000 °C.

It was discovered that pyrolysis temperature played a major factor in the morphology of wrapped-graphene sheets prepared from renewable materials without any catalyst support. Specifically, when corn husk was prepared at 800 °C, the SEM image revealed a fullerene-like morphology as displayed in Figure 45. When the temperature was increased to 900 °C, the SEM in Figure 46 showed formation of small wrapped-graphene sheets grafted on larger wrapped-graphene sheets. When pyrolysis was carried out at 1000 °C, only wrapped-graphene sheets with a hurricane shape was observed as shown in Figure 47. It appears at 800 °C, the free carbon produced from corn husk prefer to form a buckyball morphology, while at 1000 °C the free carbon assembles to form a wrapped-graphene sheets. Transmission electron micrograph of wrapped-graphene sheets prepared from corn husk at 1000 °C reveals the graphene sheets are short-range ordered and the growth pattern is possibly initiated by structural defects around the edges of the tortuous paths of the venting gas from the substrate. Figure 48 shows a TEM image of wrapped-graphene sheets prepared from corn husk at 1000 °C. The data from Table 11 shows the wrapped graphene sheets are composed of more than 92 % carbon in all cases.

Table 11. Elemental composition of wrapped-graphene sheets prepared from renewables.

Renewable	Temperature (°C)	C (at. %)	O (at. %)	P (at. %)	K (at. %)
Cassava extract	1000	98.35	1.24	0.41	-
Rice grain	1000	98.30	1.28	0.42	-
Corn grain	1000	94.75	4.98	0.26	-
Corn husk	800	92.97	7.03	-	-
Corn husk	900	93.97	5.67	-	0.36
Corn husk	1000	98.77	1.23	-	-

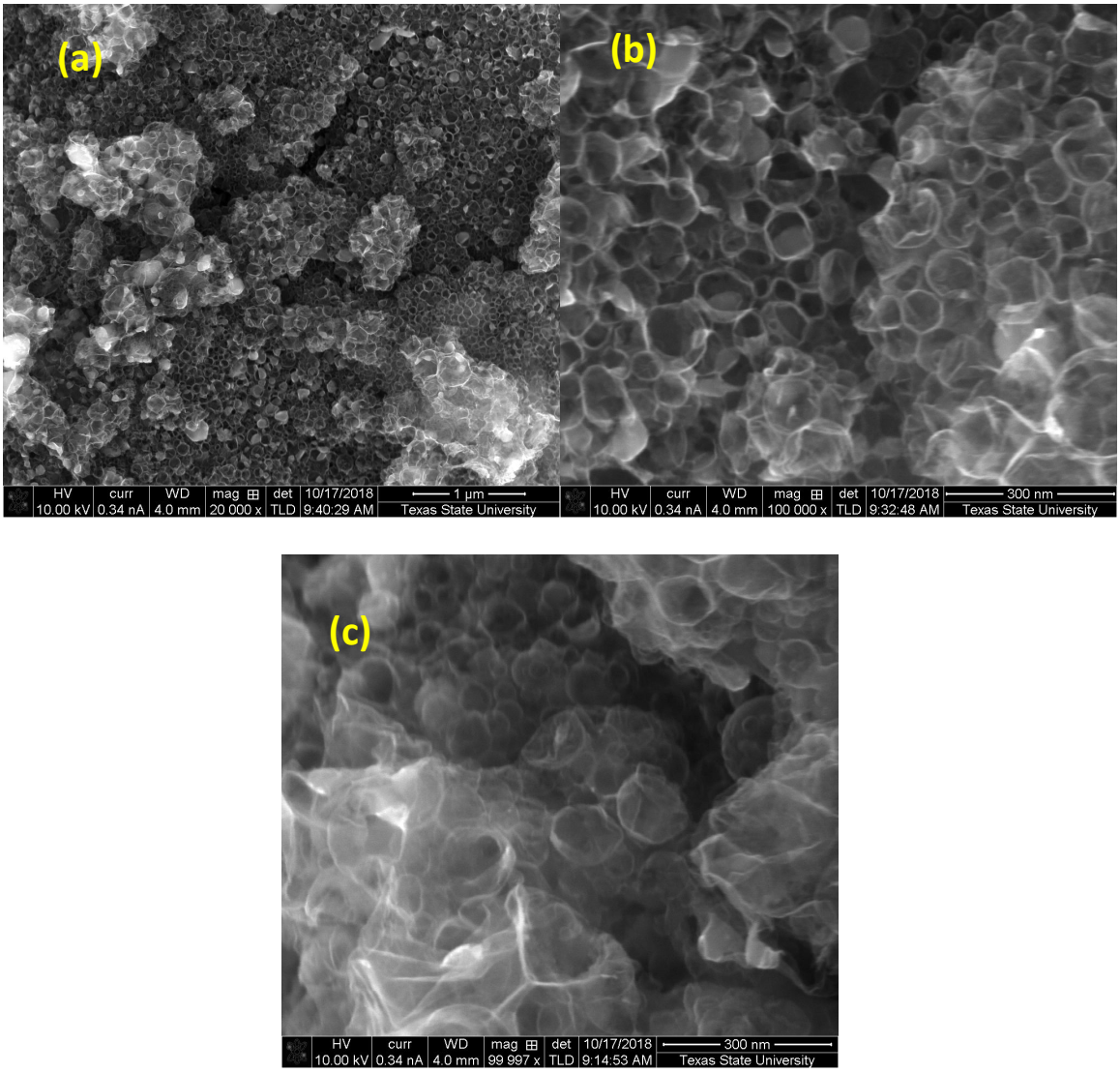

Figure 45. Scanning electron micrographs of wrapped-graphene sheets grown from corn husk only at 800 °C taken at different magnifications, (a)20,000X, (b)99,997X, and (c)100,000X.

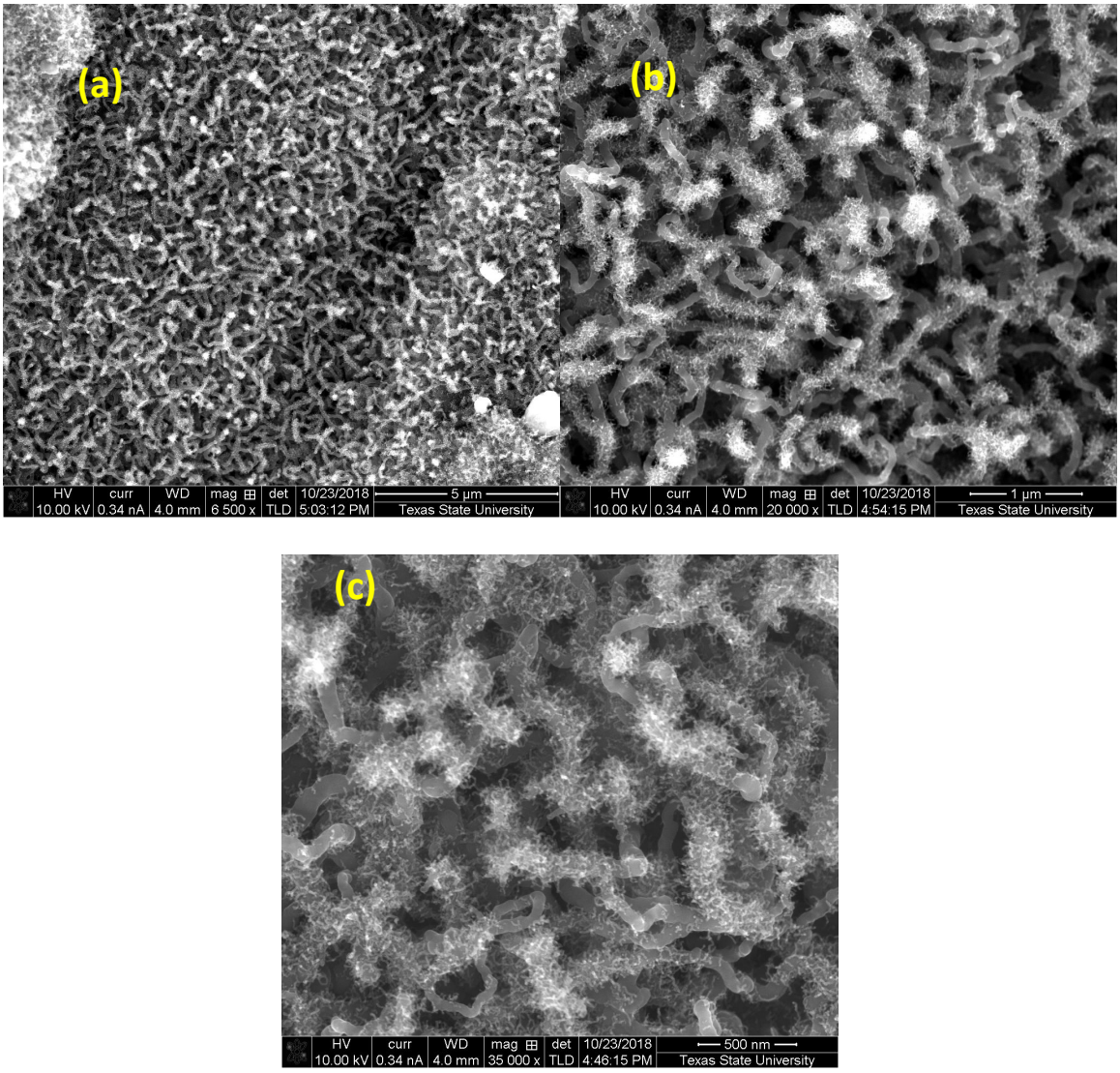

Figure 46. Scanning electron micrograph images of wrapped-graphene sheets grown from corn husk only at 900 °C taken at different magnifications, (a)6,500X, (b)20,000X, and (c)35,000X.

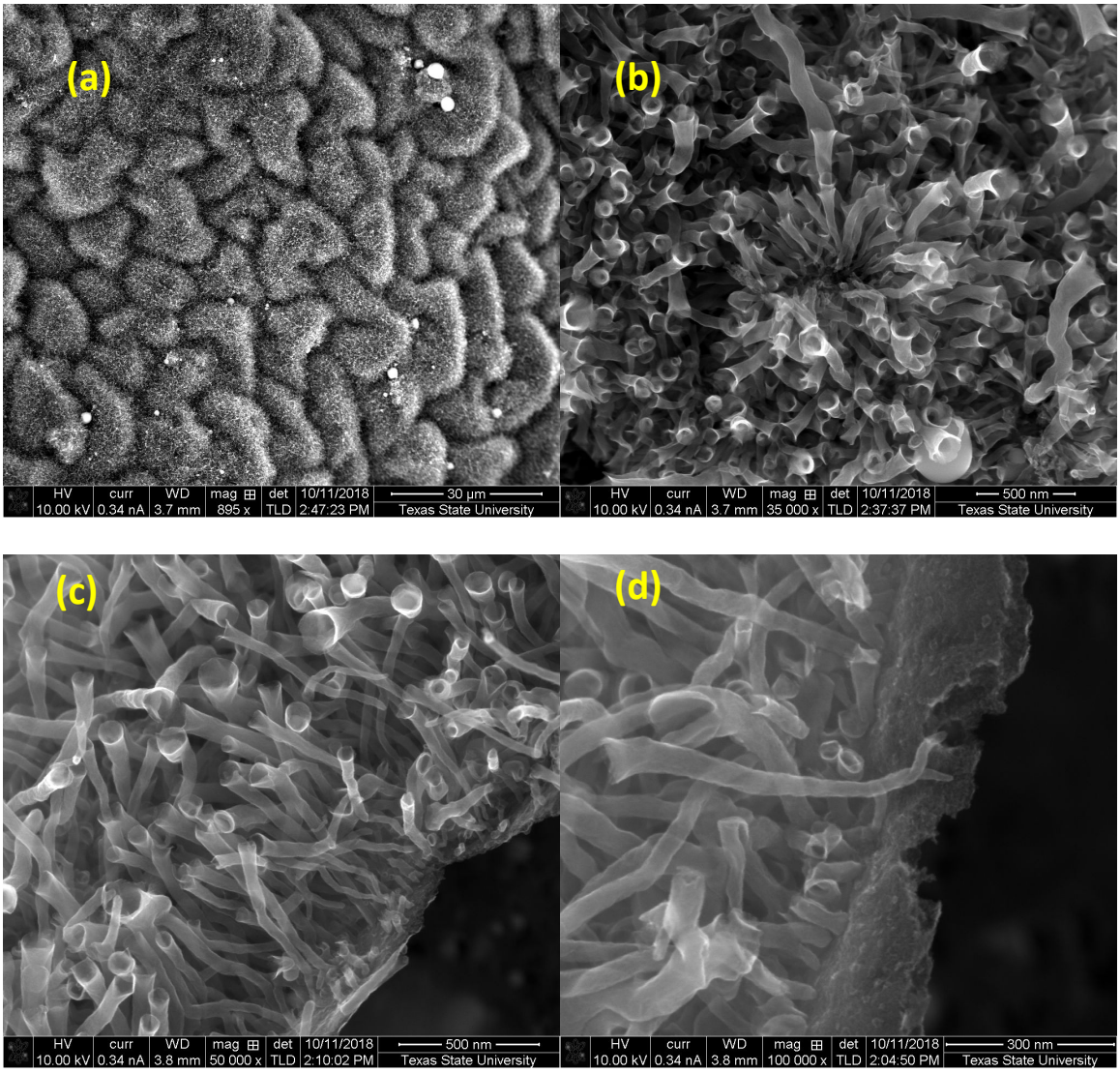

Figure 47. Scanning electron micrographs of wrapped-graphene sheets grown from corn husk grain only at 1000 °C taken at different magnifications, (a)895X, (b)35,000X, (c)50,000X, and (d)100,000X.

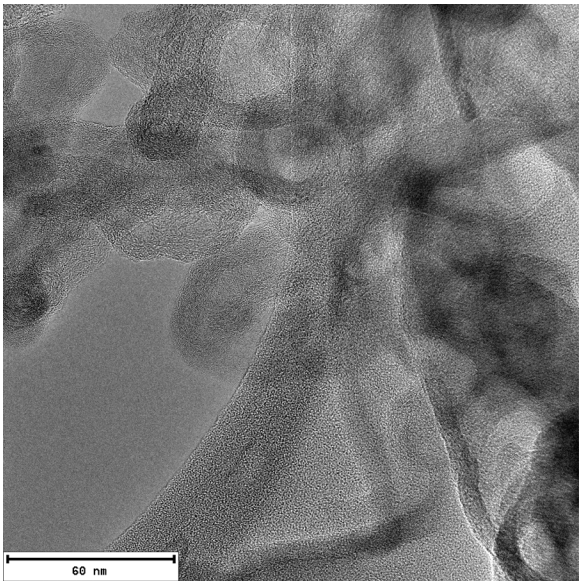

Figure 48. A transmission electron micrograph showing wrapped-graphene prepared from corn husk at 1000 °C.

5. CONCLUSIONS

The discovery of graphene sheets has attracted the interest of many researchers due to its unparalleled properties such as high surface area, carrier mobility, high flexibility, high thermal conductivity, and many more. In this research, carbon nanosheet structures were synthesized from renewable carbonaceous materials which resulted in high surface area and pore volume nanomaterials. Specifically, the formation of carbon nanosheets from cassava extract, rice grain and corn were investigated in this research. By using acid catalysts such as phosphoric acid, phosphorous acid, and/or reducing atmosphere, the resulting carbon nanosheet structures formed different morphologies.

In addition, the ratios of catalyst to carbonaceous materials were optimized for production of high surface area and large pore volume carbon nanosheets. It was observed that the acid catalysts promote gradual removal of glycosidic linkages in the carbonaceous materials to form nanosheets. In addition, the effect of thermal treatment on the formation of carbon nanosheets was explored. The data confirmed high temperature and reducing environment favor the removal of oxygen-containing groups in carbonaceous material to form sp^2 bonded carbon nanosheets.

6. FUTURE WORK

This research investigation focused on optimization of synthesis and characterization of high surface area and large pore volume carbon nanosheets from renewable carbonaceous materials. There is the need to expand the characterization of the synthesized materials to include electronic and electrical properties. In addition, the synthesized materials may have promising application for Li ion battery anode, which needs to be explored further. The high surface area and large pore volume properties of the synthesized nanosheets should also be investigated as electrode materials for ultracapacitor application. While carbon nanosheet structures may have unlimited applications, tailoring of the synthesized nanosheets by doping them with other elements or functionalizing the surfaces for certain applications such as catalysis is recommended.

APPENDIX SECTION

Data Reduction by Surface Area and Porosity Analyzer

Free Space Correction Algorithms

Free space differential compensation for the Gemini is accomplished in two steps. First, the free space correction, *Cf* (cc STP/mmHg) is determined. Second, the correction is applied to quantities adsorbed during analysis.

Determining the Free Space Correction

The free space correction *Cf* (cc STP/mmHg) is determined in of two ways: Measured or Calculated.

Measured

Evacuate the sample and balance ports, charge the reservoirs with helium, and close to 760 mmHg. Measure the gas quantity differential, *Vh* (cc STP), and the absolute sample pressure, *Ph* 9 mmHg). Record the free space.

$$Cf = \frac{Vh}{Ph}$$

Calculated

This method is calculated using a liquid nitrogen temperature. It should not be selected for free-space correction if a liquid nitrogen bath is not being used. Measure the free space correction as above, except use an empty tube of the same volume as that to be used during subsequent sample analyses.

Calculate and record the system volume correction *Vsys* (cc STP):

$$Vsys = 760 \text{ mmHg} \times \frac{Vh}{Ph}$$

Calculate the sample volume *Vsam* (cc) from independently determined sample weight *Wsam* (g) and sample density *Dsam* (g/cc):

$$Vsam = \frac{Wsam}{Dsam}$$

Calculate the quantity of gas displaced by the sample at liquid nitrogen temperature ad standard pressure:

$$Vgas = Vsam \times \frac{273.13\ K}{77.15\ K}$$

Calculate the free space correction due to both the system volume correction and the gas displaced by the sample in cc STP/mmHg.

$$Cf = \frac{Vsys - Vgas}{760\ mmHg}$$

Applying the Free Space Correction o Quantities Adsorbed

Measure the uncorrected quantity adsorbed *Vraw* (cc STP) and the pressure at which this quantity is adsorbed *Pads* (mmHg). Use the independently determined adsorbate nonideality correction *Cn* (%/atm) and the free space correction *Cf* (cc STP/mmHg) to calculate the adsorbate quantity correction correction *Vcor* (cc STP) for this point:

$$Vcor = Cf \times Pads \times \left[1 + \left(\frac{Pads \times Cn}{100\% \times \frac{760\ mmHg}{atm}}\right)\right]$$

Apply the correction to the uncorrected quantity adsorbed to obtain the correction quantity adsorbed *Vads* (cc STP):

$$Vads = Vraw - Vcor$$

BET Surface Area Calculations

For each point designed for surface area calculations, the BET transformation [68] is calculated as follows:

$$B_1 = \frac{Prel_1}{(1.0 - Prel_1)(Nads_1)}$$

where

B_1 = units of g/cm^3 STP

$Prel_1$ = relative pressure

$Naads_1$ = amount of gas adsorbed after equilibrating Ith dose (cm^3 STP)

A least-square fit is performed on the (B_1, $Prel_1$) designed paired where B_1 is dependent variable and $Prel_1$ is independent variable. The following are calculated:

- Slope (S g/cm^3 STP)
- Y-intercept (Y_{INT} g/cm^3 STP)
- Error of the slope (S_{ERR} g/cm^3 STP)
- Error of the y-intercept (YI_{ERR} g/cm^3 STP)
- Correction coefficient (C_C)

Using the results of the above calculations, the following can be calculated:

BET Surface Area (m^2/g):

$$SA_{BET} = \frac{(CSA)(6.023 \times 10^{23})}{(22414\ cm^3\ STP)(S + Y_{INT})\left(10^{18}\ \frac{nm^2}{m^2}\right)}$$

where

CSA = analysis gas molecular cross-sectional area (nm^2)

BET C value:

$$C = \frac{S + Y_{INT}}{Y_{INT}}$$

Volume of the Monolayer (cm^3/g STP)

$$V_M = [C(Y_{INT})]^{-1}$$

Error of the BET Surface Area (m^2/g):

$$BET_{ERR} = \frac{SA_{BET} \times \left({S_{ERR}}^2 + {YI_{ERR}}^2\right)^{0.5}}{Y_{INT} + S}$$

Single Point Surface Area (m^2/g):

$$S1PT = Va(1 - Pr) \times 4.35 \times \frac{CSA}{0.162}$$

where

Pr = pressure closest to 0.3 of the relative pressure points designed for surface area calculations

Va = volume corresponding to Pr

0.162 = nitrogen molecule cross-sectional area (nm^2)

Langmuir Surface Area Calculations

For each point designed for surface area calculations, the Langmuir transformation [69-70] is calculated as follows:

$$L_1 = \frac{Prel_1}{Nads_1}$$

where

L1 = units of g/cm^3 STP.

A least-square fit is performed on the (L_1, $Prel_1$) designed paired where L_1 is dependent variable and $Prel_1$ is independent variable. The following are calculated:

- Slope (S g/cm^3 STP)

- Y-intercept (Y_{INT} g/cm^3 STP)
- Error of the slope (S_{ERR} g/cm^3 STP)
- Error of the y-intercept (YI_{ERR} g/cm^3 STP)
- Correction coefficient (C_C)

Using the results of the above calculations, the following can be calculated:

Langmuir Surface Area (m^2/g):

$$SA_{LAN} = \frac{(CSA)(6.023 \times 10^{23})}{(22414\ cm^3\ STP)(S)\left(10^{18}\ \frac{nm^2}{m^2}\right)}$$

where

CSA = analysis gas molecular cross-sectional area (nm^2)

Langmuir C value:

$$C = \frac{1.0}{(Y_{INT})(V_M)}$$

Volume of the Monolayer (cm^3/g STP)

$$V_M = \frac{1.0}{S}$$

Error of the Langmuir Surface Area (m^2/g):

$$LAN_{ERR} = \frac{(SA_{LAN})(S_{ERR})}{S}$$

t-Method Calculations

For each point designed for t-method analysis, the following calculations are done:

Thickness for the Ith point:

$T_I = HP1\left[\frac{HP2}{In(Prel_I)}\right]^{HP3}$ (Halsey equation [74])

Or

$$T_I = \left[\frac{HJP1}{HJP2 - \log(Prel_I)}\right]^{HJP3}$$ (Harkins and Jura equation [72])

where

T_I = thickness for the I^{th} point

HP1 = Halsey parameter #1

HP2 = Halsey parameter #2

HP3 = Halsey parameter #3

HJP1 =Harkins and Jura parameter # 1

HJP2 =Harkins and Jura parameter # 2

HJP3 =Harkins and Jura parameter # 3

$Prel_I$ = relative pressure for the I^{th} point

A least-square analysis fit is performed on the ($Nads_I$, T_I) data pairs where $Nads_I$ is dependent variable and T_I is independent variable. Only the values of T_I between T_{MIN} and T_{MAX}, the minimum and maximum thicknesses, are used. The following are calculated:

- Slope (S cm^3/g-A STP)
- Y-intercept (Y_{INT} cm^3 /g STP)
- Correction coefficient (C_C)

Using the results of the above calculations, the following can be calculated:

External Surface Area (m^2/g):

$$SA_{EXT} = \frac{\left(S\ \frac{cm^3}{g - A}\ STP\right)(10^{10}\ \frac{A}{m})\left(D\ cm^3\ \frac{Liquid}{cm^3}\ STP\right)}{F\left(10^6\ \frac{cm^3}{m^3}\right)}$$

where

F = area correction

D = density conversion (cm^3 liquid /cm^3 STP)

Micropore Surface Area (m^2/g):

$$SA_{uP} = SA_{TOT} - SA_{EXT}$$

Where SA_{TOT} is the BET surface area if a BET report was requested, or else the Langmuir surface area.

Micropore Volume (cm^3 liquid/g):

$$V_{uP} = \left(Y_{INT}\ \frac{cm^3}{g}\ STP\right)\left(D\ \ cm^3\,\frac{liquid}{cm^3}\ STP\right)$$

Single-Point Total Pore Volume

The liquid equivalent of the designed volume adsorbed is calculated; this is the total pore volume V_{TOT} (cm^3/g):

$$V_{TOT} = (V_a)(D)$$

where

D = density conversion factor

Va = volume adsorbed

MicroPore Report

ASAP 2020 V4.03 (V4.03 E) Unit 1 Serial #: 2192 Page 1

Sample ID/Descript: Cassava extract treated with 81 % H_3PO_4 and pyrolyzed at 1000 ºC

Operator: MICHAEL

File: C:\...\OPOKU\R81P4D1K.SMP

Started: 8/2/2018 5:47:19PM Analysis Adsorptive: N2

Completed: 8/3/2018 1:21:28AM Analysis Bath Temp.: 77.238 K

Report Time: 8/3/2018 1:21:27AM Thermal Correction: No

Sample Mass: 0.0388 g Warm Free Space: 23.1409 cm^3 Measured

Cold Free Space: 66.5740 cm^3 Equilibration Interval: 30 s

Ambient Temperature: 22.00 °C Low Pressure Dose: None

Automatic Degas: No

Summary Report

Surface Area

Single point surface area at P/Po = 0.200004002: 2572.6885 m^2/g

BET Surface Area: 2625.1389 m^2/g

Langmuir Surface Area: 6046.6273 m^2/g

t-Plot Micropore Area: 162.4709 m^2/g

t-Plot External Surface Area: 2462.6680 m^2/g

BJH Adsorption cumulative surface area of pores

between 17.000 Å and 3000.000 Å width: 2831.605 m^2/g

Pore Volume

Single point adsorption total pore volume of pores

less than 0.000 Å width at P/Po = 1.000675745: 5.112336 cm^3/g

t-Plot micropore volume: 0.065579 cm^3/g

BJH Adsorption cumulative volume of pores

between 17.000 Å and 3000.000 Å width: 5.291191 cm^3/g

Pore Size

Adsorption average pore width (4V/A by BET): 77.8981 Å

BJH Adsorption average pore width (4V/A): 74.745 Å

DFT Pore Size

Volume in Pores < 18.09 Å : 0.48551 cm^3/g

Total Volume in Pores <= 387.34 Å : 3.58323 cm^3/g

Area in Pores > 387.34 Å : 0.000 m^2/g

Total Area in Pores >= 18.09 Å : 1015.889 m^2/g

DFT Surface Energy

Total Area : 2573.750 m^2/g

Nanoparticle Size

Average Particle Size 22.856 Å

Horvath-Kawazoe

Maximum pore volume at P/Po = 0.983722082: 5.047021 cm^3/g

Median pore width: 149.175 Å

REFERENCES

1. E. Gerstner, “Nobel Prize 2010: Geim and Novoselov,” Nature Physics, Advance online Publication, 2010.

2. A. K. Geim and K. S. Noveselov, “The rise of graphene,” Nature Materials, 6, 2007, 183-191.

3. J. C. Meyer *et al.*, “The structure of suspended graphene sheets,” Nature Letters, 446, 2007, 60-63.

4. A. K. Geim, “Graphene: status and prospects” Science, 324, 2009, 1530 – 1534.

5. K. S. Novoselov *et al.*, “A roadmap for graphene,” Nature Review, 490, 2012, 192-200.

6. A. C. Ferrari *et al.*,”Science and technology roadmap for graphene, related two-dimensional crystals, and hybrid systems,” Nanoscale, 7 (11), 2015, 4598-4810.

7. C. N. R. Rao *et al.*, “Synthesis, characterization and selected Properties of graphene,” Graphene: Synthesis, Properties, and Phenomena, Chapter 1, 1st Ed., ©2013 Wiley-VCH Verlag GmbH & Co. KGaA.

8. Z. Li *et al.*, “Superstructured assembly of nanocarbons: fullerenes, nanotubes, and graphene, Chemical Reviews, 115, 2015, 7046-7117.

9. D. R. Dreyer, S. Park, C. W. Bielawski, and R. S. Ruoff, “The chemistry of graphene oxide,” Chem. Soc. Rev., 39, 2010, 228-240.

10. Y. Jiang, *et al.*, “Versatile Graphene Oxide Putty-Like Material, Advanced Materials, 28 (46), 2016, 10287-10292.

11. H. Cheng *et al.*, “Graphene fiber: a new material platform for unique applications, NPG Asia Materials, 6, 2014, 1-13.

12. K. S. Novoselov, “Graphene mind the gap,” Nature Materials, 6, 2007, 720-721.

13. S. Zhou *et al.*, “Substrate-induced bandgap opening in epitaxial graphene,” Nature Materials, 6, 2007, 770–775.

14. K. S. Novoselov *et al.*, “Electric field effect in atomically thin carbon films,” Science, 306, 2004, 666-669.

15. K. S. Novoselov *et al.*, “Room-temperature quantum hall effect in graphene,” Science, 10, 2007, 1.

16. T. Ando, “The electronic properties of graphene and carbon nanotubes,” NPG Asia Materials, 1, 2009, 17-21.

17. J. Zhang *et al.*, “Tunable electronic properties of graphene through controlling bonding configurations of doped nitrogen atoms,” Scientific Reports, 6, 2016, 28330-28340.

18. L. A. Ponomarenko *et al.*, “Tunable metal-insulator transition in double-layer graphene heterostructures,” Nature Physics, 7, 2011, 958-961.

19. K. Kim *et al.*,”A role for graphene in silicon-based semiconductor devices,” Nature, 479, 2011, 338-344.

20. F. Schwierz, “Graphene transistors,” Nature Nanotechnology, 5, 2010, 487-496.

21. M. Zhao et. al, “large-scale chemical assembly of atomically thin transistors and circuits,” Nature Nanotechnology, 11, 2016, 954-960.

22. G. Wang *et al.*, “Direct Growth of Graphene Film on Germanium Substrate,” Scientific Reports, 3, 2013, 2465-2471.

23. T. J. Echtermeyer *et al.*, “Strong plasmonic enhancement of photovoltage in graphene,” Nature Communications, 2, 2011, 458-463.

24. Q. Miao *et al.*, “Magnetic properties of N-doped graphene with high curie temperature,” Scientific Reports, 6, 2016, 21832-21842.

25. A. A. Balandin, “Thermal properties of graphene and nanostructured carbon materials,” Nature Materials, 10, 2011, 569-581.

26. F. Schedin et. al, “Detection of individual gas molecules adsorbed on graphene,” Nature Materials, 6, 2007, 652-655.

27. D. Deng et. al, “Catalysis with 2D materials and their heterostructures,” Nature Nanotechnology, 11, 2016, 218-230.

28. J. Hu *et al.*, “Rippling ultrafast dynamics of suspended 2D monolayers, graphene,”PNAS, 2016, E6555-E6561.

29. C. Lu *et al.*, “A comparison of the elastic properties of graphene – and fullerene-reinforced polymer composites: the role of filler morphology and size,” Scientific Reports, 6, 2016, 31735-31744.

30. P. Samri *et al.*, “Graphene-based nanocomposites for structural and functional applications: using 2-dimensional materials in a 3-dimensional world,” 2D Materials, 2, 2015, 30205-30211.

31. S. Park, “The puzzle of graphene commercialization,” Nature Reviews - Materials, 1, 2016, 16085-16096.

32. S. Park, “Graphene for Electronic Devices,” Samsung Advanced Institute of Technology, 2015

33. W. Liu, S. Chai, A. Mohamed, and U. Hashim, “Synthesis and characterization of graphene and carbon nanotubes: A review on the past and recent developments,” J. of Industrial and Eng. Chem., 20, 2014, 1171-1185.

34. S. Park and R. S. Ruoff, “Chemical methods for the production of graphenes,” Nature Nanotechnology, 4, 2009, 217-224.

35. S. Gambhir, R. Jalili, D. L. Officer, and G. G. Wallace, “Chemically converted graphene: scalable chemistries to enable processing and fabrication,” NPG Asia Materials, 7, 2015, 1-15.

36. H. C. Lee *et al.*, “Synthesis of single-layer graphene: A review of recent development,” Procedia Chemistry, 19, 2016, 916-921.

37. R. Yadav and C. K. Dixit, ”Synthesis, characterization and prospective applications of nitrogen-doped graphene: A short review,” J. of Science: Advanced Materials and Devices, 2, 2017, 141-149.

38. A. Dato and M. Frenklach, “Substrate-free microwave synthesis of graphene: experimental conditions and hydrogen precursors,” New J. of Physics, 12, 2010, 125013-124037.

39. J. Xia, F. Chen, J. Li, and N. Tao, “Measurement of the quantum capacitance of graphene,” Nature Nanotechnology, 4, 2009, 505-509.

40. H. Kim, K. Park, J. Hong and K. Kang “All-graphene-battery: bridging the gap between supercapacitors and lithium ion batteries,” Science reports, 4, 2014, 5278, 1-8.

41. M. Pumera, “Electrochemistry of graphene, graphene oxide, and other graphenoids; Review,” Electrochemistry Comm., 36, 2013, 14-18.

42. R. Raccichini *et al.*, “The role of graphene for electrochemical energy storage,” Nature Materials. 14, 2015, 271-279.

43. A. Munzer *et al.*, “All gas-phase synthesis of graphene: characterization and its utilization for silicon-based lithium-ion batteries,” Electrochimica Acta 272, 2018, 52-59.

44. A. Amiri *et al.*, "Mass production of highly porous graphene for high performance supercapacitors," Scientific Reports, 6, 2016, 32686-32697.

45. X. Shi *et al.*, "Recent advances of graphene-based materials for high-performance and new-concept supercapacitors," J. of Energy Chemistry, 27, 2018, 25-42.

46. I. Childres et. al, "Raman spectroscopy of graphene related materials," NOVA, Chapter 19, 1-20. https://www.novapublishers.com/catalog/product_info.php?products_id=41276

47. A. C. Ferrari et. al, "The Raman fingerprint of graphene," Phys. Rev. Lett., 97, 2006, 187401, 1-5.

48. A. C. Ferrari and J. Robertson, " Intrepretation of Raman spectra of disordered and amorphous carbon, " Physical Review B, 61 (20), 2000, 14095-14107.

49. I. Childres *et al.*, "Raman Spectroscopy of graphene and related materials," New Developments in Photon and Materials Research edited by J. I. Jang, Nova Science, Chapter 19, 2013, ISBN: 978-1-62618-384-1.

50. M. Reininghaus *et al.*," Laser induced non-thermal deposition of ultrathin graphite," Appl. Phys. Lett., 100, 2012, 151606.

51. S. Dhar *et al.*, "A new route to graphene layers by selective laser ablation," AIP Adv., 1, 2011, 022109.

52. S. Z. Mortazavi *et al.*, "Fabrication of graphene based on Q-switched Nd:YAG laser ablation of graphite target in liquid nitrogen Fabrication of graphene," Laser Phys. Lett., 9, 2012, 547–552.

53. J. Israelachvili, Intermolecular and surface force, Academic Press, Boston, 3rd Ed., 2011.

54. F. Bonaccorso *et al.*, “Production and processing of graphene and 2d crystals,” Mater. Today, 15, 2012, 564– 589

55. B. C. Brodie,’ Sur le poids atomique du graphite,” Ann. Chim. Phys., 59, 1860, 466.

56. L. V. Staudenmaier, “Verfahren zur Darstellung der Graphitsäure,” Ber. Dtsch. Chem. Ges., 31, 1898, 1481.

57. G. Ruess and F. Vogt, “Höchstlamellarer Kohlenstoff aus Graphitoxyhydroxyd.,” Monatsh. Chem., 78, 1948, 222.

58. W. S. Hummers and R. E. Offeman,” Preparation of Graphitic Oxide,” J. Am. Chem. Soc., 80, 1958, 1339–1339.

59. L. Royer,”Experimental research on epitaxy or mutual orientation of crystals of different species,” Bull. Soc. Fr. Min., 51, 1928, 7.

60. J. Hass *et al.*, “Highly ordered graphene for two dimensional electronics,” Appl. Phys. Lett., 2006, 89, 143106–143103.

61. J. Hass *et al.*, “Interface structure of epitaxial graphene grown on 4H-SiC(0001),” Phys. Rev. B, 78, 2008, 205424.

62. T. B. Massalski *et al.*, Binary Alloy Phase Diagrams, ASM International, 1990

63. H. Okamoto, Phase Diagrams for Binary Alloys, Desk Handbook, vol. 1, 2000.

64. Y. Gamo *et al.*, “Atomic structure of monolayer graphite formed on Ni(111),” Surf. Sci., 374, 1997, 61–64.

65. S. Bae *et al.*, “Roll-to-roll production of 30-inch graphene films for transparent electrodes,” Nat. Nanotechnol., 5, 2010, 574–578.

66. A. C. Ferrari, “Raman spectroscopy of graphene and graphite: Disorder, electron–phonon coupling, doping and nonadiabatic effects,” Solid State Communications, 143, 2007, 47–57.

67. J. Pokrzywinsk *et al.*, “Unrivaled combination of surface area and pore volume in micelle-templated carbon for supercapacitor energy storage,” J. Mater. Chem. A, 5, 2017, 13511–13525.

68. Beall et al., “Single crystalline graphene synthesized by thermal annealing of humic acid over copper foils,” Physica E: Low-dimensional Systems and Nanostructures, 56, 2014, 331-336.

69. Powell and Beall, “Graphene oxide and graphene from low grade coal: Synthesis, characterization and applications,” Current Opinion in Colloid & Interface Science, Vol. 20, 5–6, 2015, 362-366.

70. T. F. Emirua and D. W. Ayele, “Controlled synthesis, characterization and reduction of graphene oxide: A convenient method for large scale production,” Egyptian Journal of Basic and Applied Sciences, 4 (1), 2017, 74-79.

71. S. Brunauer, P.H. Emmett, and E. Teller, Adsorption of gases in multimolecular layers, J. Am. Chem. Soc., 60, 1938, 309-319.

72. I. Langmuir, The constitution and fundamental properties of solids and liquids: Part I. Solids, J. Am. Chem. Soc., 38, 1916, 2221–2295.

73. I. Langmuir, The adsorption of gases on plane surfaces of glass, mica and platinum, J. Am. Chem. Soc., 40, 1918, 1361–1403.

74. G. Halsey, Physical adsorption on non-uniform surfaces, J. Chem. Phys., 16, 1948, 931-937.

75. W. D. Harkins, and G. Jura, An adsorption method for the determination of the area of a solid without the assumption of a molecular area, and the area occupied by nitrogen molecules on the surfaces of solids, J. Chem. Phys., 11, 1943, 431-432.

76. J. Kelvin, (Published under the name of Sir Williams Thomson), On equilibrium of vapor at a curved surface of liquid, Phil. Mag., 42, 1871, 448-452.

77. E. P. Barrett, L. S. Joyner, and P. P. Helenda, The determination of pore volume and area distributions in porous substances, I, computations from nitrogen isotherms, J. Am. Chem. Soc., 73, 1951, 373-380.

78. J. M. Schopf, "Definitions of peat and coal and of graphite that terminates the coal series (graphocite)," The Journal of Geology, 74 (5), 1966, 584-592.

79. Georg et. al., "Promotion of graphite formation by tectonic stress – a laboratory experiment," Geophysical Journal International, 160 (3), 2005, 1059–1067.

80. Generalic, Eni. "Starch." Croatian-English Chemistry Dictionary & Glossary. 20 Oct. 2018. KTF-Split. 4 Nov. 2018)

81. P. Scherrer, "Bestimmung der Grösse und der inneren Struktur von Kolloidteilchen mittels Röntgenstrahlen," Nachr. Ges. Wiss. Göttingen, 26, 1918, 98-100.

82. L. Estavez at al., Hierarchically Porous Graphitic Carbon with Simultaneously High Surface Area and Colossal Pore Volume Engineered via Ice Templating, ACS Nano, 11, 2017, 11047-11055.

83. A. Cuesta *et al.*, Raman Microprobe Studies on Carbon Materials, Carbon, 32, 1994, 1523−1532.

84. M. S. Dresselhaus, Perspectives on Carbon Nanotubes and Graphene Raman Spectroscopy, Nano Lett., 10, 2010, 751−758.

85. R. Sahore et. al. Design Principles for Optimum Performance of Porous Carbons in Lithium−Sulfur Batteries. Adv. Energy Mater., 6, 2016, 1600134.